ChemElectroChem

Review
doi.org/10.1002/celc.202300512

Chemistry Europe
European Chemical Societies Publishing

www.chemelectrochem.org

Defective Carbon for Next-Generation Stationary Energy Storage Systems: Sodium-Ion and Vanadium Flow Batteries

Sophie McArdle,*[a] Felix Bauer,[b] Simone Fiorini Granieri,[c, d, e] Marius Ast,[b] Fabio Di Fonzo,[c, d] Aaron T. Marshall,[a] and Hannes Radinger*[f]

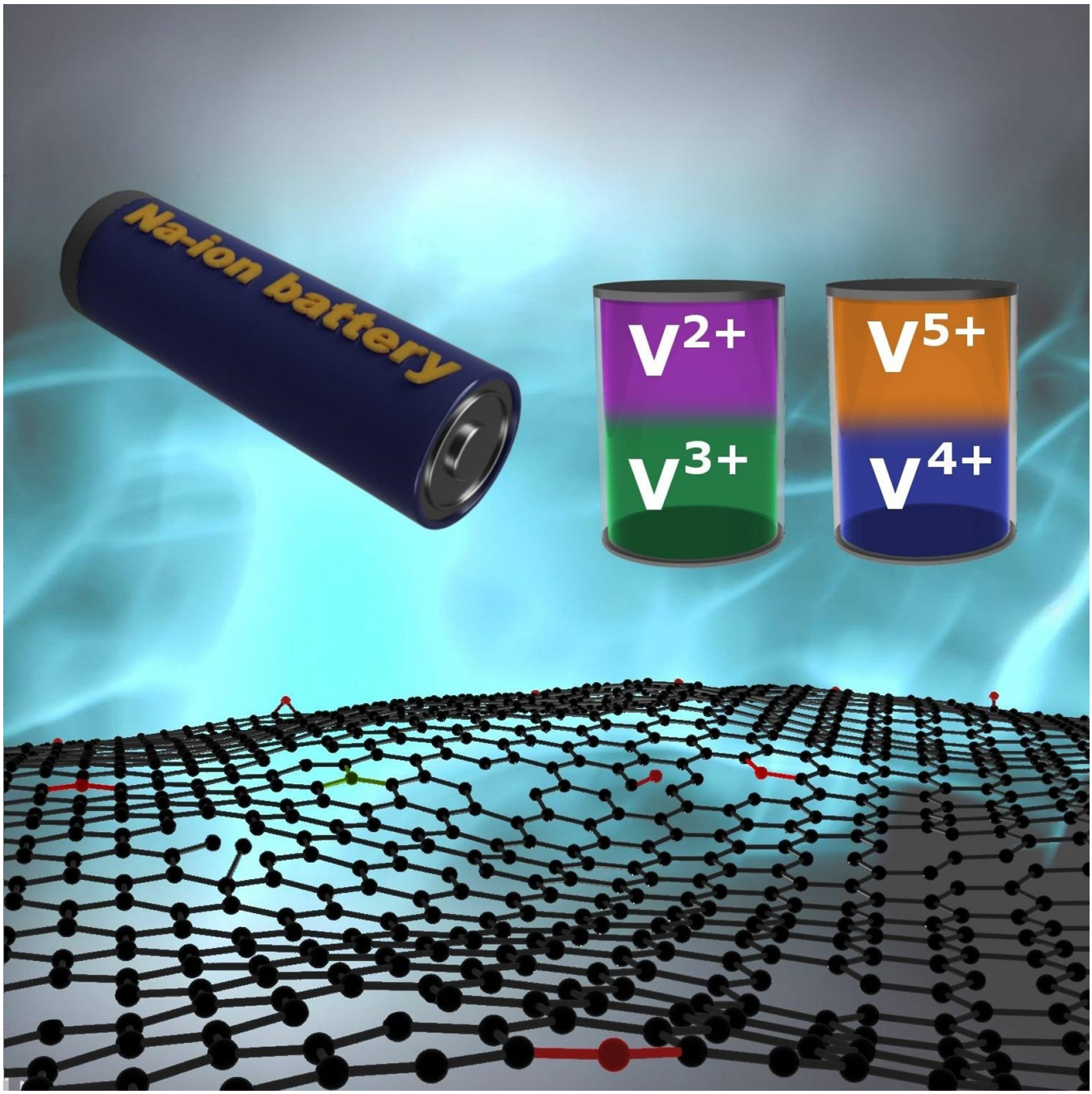

This review examines the role of defective carbon-based electrodes in sodium-ion and vanadium flow batteries. Methods for introducing defects into carbon structures are explored and their effectiveness in improving electrode performance is demonstrated. In sodium-based systems, research focuses primarily on various precursor materials and heteroatom doping to optimise hard carbon electrodes. Defect engineering increases interlayer spacing, porosity, and changes the surface chemistry, which improves sodium intercalation and reversible capacities. Heteroatom functionalisation and surface modification affect solid electrolyte interface formation and coulombic efficiencies. For flow batteries, post-fabrication electrode enhancement methods produce defects to improve electrode kinetics, although these methods often introduce oxygen functional groups as well, making isolation of defect effects difficult. Continued research efforts are key to developing carbon-based electrodes that can meet the unique challenges of future battery systems.

1. Introduction

The shift towards renewable energy replacing fossil fuels has created a large demand for efficient energy storage, which has triggered substantial research efforts in the field of advanced battery technologies.[1] Recent research has put an emphasis on cheaper and safer alternatives to replace the already utilised lithium-ion battery,[2] with two promising candidates being sodium-ion batteries[3] (SIB) and vanadium flow batteries[4] (VFB). Thus, extensive research into developing the various components of SIBs and VFBs has been carried out to enhance battery performance and reduce cost, with considerable attention paid to improving the electrodes.[5,6] These electrodes are generally carbon-based, specifically hard carbon (HC) for SIBs and carbon fibres (felt or paper) for VFBs, where the high electrical conductivity, tuneable surface chemistry, and abundance make it an attractive electrode material for these electrochemical devices.[7]

Carbon electrodes enable a variety of charge storage mechanisms, ranging from intercalation and adsorption to pseudo-capacitance.[8] Although SIBs and VFBs are both energy storage technologies, the properties and functionality required for the electrode material of each battery is different. Importantly, carbon-based materials can be fine-tuned in order to exhibit a combination of these desired characteristics, which makes it incredibly versatile and important to investigate. Reviewing the electrode mechanisms and performance of two different battery technologies allows for an interesting perspective on the functionality of carbon and highlights the importance of carbon electrodes for the future of renewable energy technologies. Studies often report on methods to enhance these mechanisms for battery technologies, such as via electrode surface modification, electrode precursor selection, or the use of electrocatalysts.[9–12] For SIBs, work is often done to improve sodium intercalation and storage, formation of the solid electrolyte interface, and initial coulombic efficiency (ICE), which may be achieved by altering the surface chemistry, micro-porosity, interlayer spacing, and curvature of the carbon electrode.[9,10] VFB electrode performance can be improved by introducing "active sites" or modifying the electrode structure to better facilitate the vanadium redox reactions through increased charge transfer, electrochemically-active surface area, conductivity, and wettability.[11,12] From this research, the presence of defects within the carbon structure has been reported to influence the electrochemical behaviour of electrodes for both SIBs[13–17] and VFBs.[18–22]

Both SIBs and VFBs have the potential to replace lithium-ion technology concurrently for residential, commercial, and grid-scale energy storage. Thus, it is especially important to review the most recent advances and future direction of these two technologies in order to work towards this. Herein, this review aims to address the relationship between defective carbon-based materials and the electrochemical processes inherent in these battery systems, as well as explain the fundamental mechanisms that underpin their performance. This review is structured into several sections, each focusing on a specific aspect of defective carbon materials and their relevance to energy storage applications. Section 2 deals with the fabrication and processing of defective carbon materials in SIBs and VFBs. Section 3 explores the influence of precursor material selection and heteroatom doping for SIBs, specifically how electrode surface modifications impact sodium intercalation, formation of the solid electrolyte interface, and the ICE. Section 4 investigates how VFB electrode characteristics, such as the charge transfer rate, can be improved *via* defect engineering and heteroatom functionalisation. Finally, insights into the mechanisms and future direction for the fabrication and performance

[a] *S. McArdle, Prof. Dr. A. T. Marshall*
Department of Chemical and Process Engineering
The MacDiarmid Institute of Advanced Materials and Nanotechnology
University of Canterbury
Christchurch, 8140 (New Zealand)
E-mail: sophie.mcardle@pg.canterbury.ac.nz

[b] *F. Bauer, M. Ast*
Institute for Applied Materials
Karlsruhe Institute for Technology
Eggenstein-Leopoldshafen, 76344 (Germany)

[c] *S. F. Granieri, Dr. F. Di Fonzo*
Italian Institute of Technology
Milano (MI), via rubattino 81, 20134 (Italy)

[d] *S. F. Granieri, Dr. F. Di Fonzo*
X-nano srl, Milano (MI)
via rubattino 81, 20134 (Italy)

[e] *S. F. Granieri*
Politecnico di Milano, Department of Energy
via lambruschi 4, Milano (MI), 20156 (Italy)

[f] *Dr. H. Radinger*
Siemens AG
Schuckertstr. 2, 91058 Erlangen (Germany)
E-mail: hannes.radinger@siemens.com

of defective carbon electrodes for battery storage technologies is discussed.

1.1. Defect classifications and their functionality

Defects in carbon-based materials can be categorised as either intrinsic or non-intrinsic (also referred to as doping defects).[23,24] Intrinsic defects include those induced within the carbon lattice, such as lattice distortions, carbon vacancies, and edge defects (such as zigzag and armchair edges). Doping defects refer to those formed because of heteroatom or metal doping, and can result in heteroatom-carbon bonds, heteroatom vacancies (similar to a carbon vacancy defect), and changes in the carbon matrix. The catalytic nature of defective carbon is extensively reported for other electrochemical systems, such as CO_2 reduction, nitrogen reduction, and the oxygen and hydrogen evolution reactions,[25,26] and can provide additional insight into how defects may behave as redox-active sites.

Edge defects, such as zigzag and armchair edges (Figure 1a), have high spin and charge density due to the configuration of carbon atoms.[23] The local charge redistribution is thought to saturate the edge sites with electrons, hence, providing sites for better charge transfer.[27] Carbon vacancies refer to an absence of one (vacancy) or multiple (hole) carbon atoms in the matrix (Figure 1b), and therefore act in a similar way to edge defects due to the carbon edges formed around the carbon vacancy or hole.[27] Carbon vacancies can also lead to further deformation of the adjacent carbon atoms, with two out of the three dangling bonds present forming a weak bond between two

Sophie McArdle is currently a PhD candidate at the University of Canterbury, New Zealand. Here, she also received a Bachelor of Chemical and Process Engineering (Hons) with a minor in Energy Processing Technologies. Her PhD project focuses on modifying electrodes to enhance the performance of redox flow batteries. Her research interests include electrochemistry, renewable energy technologies, and energy storage.

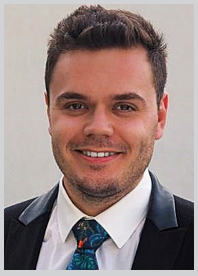

Felix Bauer received both his bachelor and master degrees in chemistry from the Karlsruhe Institute of Technology. During his master's program, he worked as a student assistant, specializing in vanadium flow batteries. His master's thesis was centred on dendrite growth in sodium metal batteries. Since 2023, he is a PhD student focusing on the surface properties of hard carbon anodes in sodium-ion batteries, contributing to the development of sustainable energy solutions.

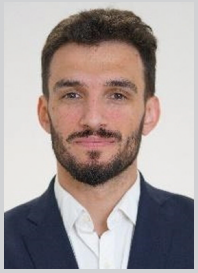

Simone Fiorini Granieri is a PhD student at the Politecnico di Milano. He obtained his bachelor's degree in Materials Science from the University of Milano-Bicocca, Italy, and his master's degree in Materials & Nanotechnology Engineering from the Politecnico di Milano, Italy. His PhD research, carried out in collaboration with the Italian Institute of Technology and Flow-nano, deals with the fabrication of novel nanocarbon catalysts for energy storage systems. He is also a senior researcher at Flow-nano.

Marius Ast completed his bachelor and master theses in chemistry at the Karlsruhe Institute of Technology. His master thesis concentrated on heteroatom doping for hard carbon anodes in sodium-ion batteries. Since 2023, his main research as part of his PhD is focused on sodium-ion storage properties of hard carbon anodes.

Dr. Fabio Di Fonzo is the co-founder, president and CSO/CTO of X-nano and Flow-nano. He got his PhD in Radiation Science and Technology from the Nuclear Engineering Department of the Politecnico di Milano University, Italy, and two MS in Mechanical Engineering from the University of Minnesota, US, and from the Politecnico di Milano University, Italy, (Energy Major). Fabio has worked on functional nanomaterials for 20 years.

Aaron Marshall is a Professor in Chemical and Process Engineering at the University of Canterbury, New Zealand. He received bachelor and master degrees from Massey University in New Zealand and a PhD from the Norwegian University of Science and Technology. Professor Marshall specialises in electrochemical engineering and currently works on flow batteries, water electrolysis, CO_2 reduction and molten oxide electrolysis. Professor Marshall has co-founded two companies related to his research and is passionate about converting science into practical applications which can make a difference.

Hannes Radinger studied materials science and energy technology at the University of Augsburg and Technical University Darmstadt before receiving his PhD in 2022 from the Karlsruhe Institute of Technology with a thesis on redox flow batteries. Stays as a visiting scientist at the Technical University of Denmark and postdoc at the University of Canterbury, New Zealand, complemented his scientific career. Since 2023, he has been working as a R&D engineer for energy storage systems at Siemens AG in Erlangen.

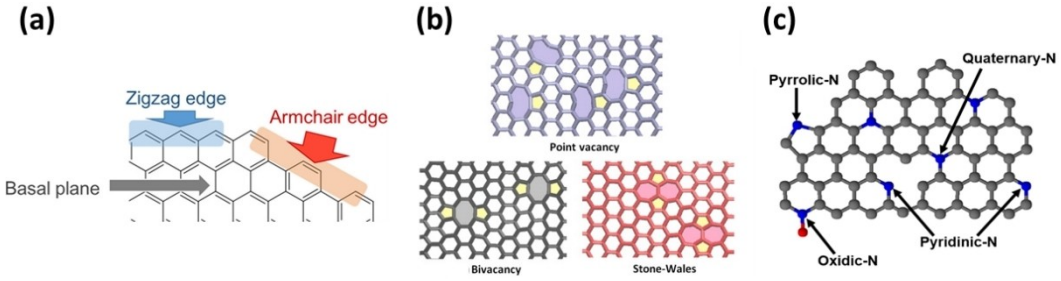

Figure 1. (a) Schematic of graphene with basal plane, zigzag edge, and armchair edge carbon bonding. Reprinted with permission from ref. [165] Copyright (2018) ACS. (b) Different types of carbon vacancies. Reprinted with permission from ref. [166] Copyright (2013) Elsevier. (c) Structure of different nitrogen functionalities. Reprinted with permission from ref. [51] Copyright (2020) Elsevier.

adjacent carbon atoms, leaving one dangling bond. It is thought that the higher local charge density of the carbon atoms surrounding the vacancy improves the reactivity towards redox species.[28]

Heteroatom doping defects can also alter the carbon lattice structure and local chemical reactivity due to changes in the carbon bonding.[29] Bonds formed between the heteroatom and carbon atoms can exhibit similar behaviour to intrinsic carbon defects, such as changes in charge distribution and lattice structure. For example, nitrogen doping is thought to allow N-doped sites to carry a positive charge density and higher electron spin density to promote better electron transfer due to the higher electronegativity of nitrogen compared to carbon.[30] However, the configuration of various groups formed due to heteroatom doping (e.g. quaternary-N, pyrrolic-N, and pyridinic-N groups from N-doping (Figure 1c)) will influence its structure and effect on charge density.

Although both intrinsic and heteroatom doping defects are reported on for the sodium-ion and vanadium flow battery electrodes, the functionality of these defective carbon sites at the electrode surface differs slightly. For sodium-ion batteries, defects are thought to provide sites for sodium intercalation and increase the ICE.[31] For vanadium flow batteries, defect sites have been reported to enhance electron transfer and increase the electrochemically-active surface area.[18,32,33]

2. Manufacturing and microengineering of defective carbon

The development of energy storage technologies has focused heavily on creating economical, sustainable, and highly efficient systems such as SIBs and VFBs. The choice of electrode material has a significant impact on the overall performance. Carbon-based electrodes are commonly used because they are inexpensive, have good chemical stability and electrical conductivity, and can be easily modified. However, their poor electrochemical performance requires the use of large amounts of material, adding to the cost of the system. Thus, defective carbon materials have been studied in detail for their potential to improve the performance of these batteries.[34]

The different functions of the defects in the carbon structure can vary from VFB to SIB due to the electrochemical mechanisms occurring at the electrode interface and are discussed in the corresponding sections of this paper. In general, defects tend to lower the energy barrier of the electrochemical phenomena, *i.e.*, absorption and chemical reaction, by changing the energy band around the Fermi level.[35]

The perfect graphene structure has a symmetric electron/hole dispersion spectrum around the zero point, which leads to the well-known zero-gap semiconductor behaviour. The introduction of structural defects into the lattice of the structure causes the symmetry of the electron hole to be broken, leading to the breaking of the electrical neutrality of graphene.[26] The introduction of defects therefore results in lower electrical conductivity, which can affect the overall performance and practical potential as an electrode. However, the introduction of defects usually occurs in the first few nanometres of the carbon surface, while the main material, which contributes the most to electrical conductivity, is not altered by the process.

2.1. Electrodes in Vanadium Flow Batteries

Electrodes in VFBs must possess the above-mentioned properties to ensure optimal performance, durability, and reliability of the battery. Commercially available electrodes are usually carbon felt (CF), graphite felt (GF), carbon paper (CP) and carbon cloth, as they represent a good compromise between these requirements. To further improve these properties, research has focused on morphological and chemical-structural modifications of the electrodes, such as defects and functional groups. The two main approaches for electrode modification include additive and subtractive methods. Alternatively, it is possible to replace conventional felt, paper or cloth electrodes with a new carbon mat specifically designed for with better performance in VFBs. The latter method offers the possibility of fine-tuning fibre properties, dramatically increasing surface area and defects in the structure, and also improving electrolyte diffusion.[36] In this section, different fabrication methods and engineering processes for the production of defected electrodes for VFBs are compared by cell performances. Electrode performances are affected by several experimental factors, such

as geometrical cell area, flux velocity, choice of the ionic membrane, flow-field geometry, cut-off potential and electrolyte concentration; therefore, a performance comparison is not trivial. Moreover, differences in experimental conditions complicate the understanding of micro-structural effects from macro-structural ones. A standardisation of experimental procedures would be beneficial for the scientific community. Table 1 shows the results, in terms of current density, from various works along with some experimental conditions. The scope of the research was limited to CF and GF electrodes in order to increase the correlation between the different methods and the final performances. However, other substrates such as CP[37] have often been used as a starting point for the introduction of defects.

2.1.1. Subtractive methods

Subtractive processes remove material from the surface, resulting in the formation of defects and reactive dangling bonds that react with the environment to form functional groups. Additionally, the overall roughness is increased, and the surface area is maximised. Subtractive methods are usually performed *via* thermal treatment in different atmospheres,[38–41] plasma[42–45] and chemical etching.[19,46] Despite the low cost and scalability of this method, the resulting material cannot be precisely controlled, leading to a mixture of defects and functional groups randomly distributed in the structure. The quantity and type of defects strongly depend on the method used. In subtractive methods, the oxidation reaction of the carbon is utilised to form volatile compounds, causing the carbon structure to form intrinsic defects, *i.e.*, edge sites, vacancies, grain boundaries, dislocations, cracks and void defects. The resulting carbon lattice, which consists of multiple dangling bonds, undergoes structural reorganisation to lower its energy state by changing the bond geometry around the vacancy as the carbon atoms are removed from the lattice.[47] In general, this leads to the formation of sp^3 carbon allotropes around the vacancies, breaking the coplanarity of the six-atom carbon ring and redistributing the electronic charge, which improves the electrochemical properties.[48] Doping with heteroatoms is usually present when the subtractive processes are carried out in a reactive environment, *e.g.*, with oxygen, nitrogen (if plasma or chemically assisted) and sulphur functional groups. These functionalities can be in-plane, as in the case of nitrogen and sulphur, or out-of-plane, as in the case of oxygen. Both in-plane and out-of-plane functionalities tend to distort the carbon structure and its electronic cloud due to the different electronegativity, which increases the electrochemical performances and reactivity.[49]

By thermally treating a graphite felt (GF) in ambient air at 500 °C for 8 h, Jiang *et al.*[38] achieved a so-called multiscale GF with an enhanced current density of 400 mA cm^{-2} at an energy efficiency of ~81 %. The treatment increased the surface area by more than 96-fold to ~167 m^2 g^{-1} due to the formation of voids in the fibres, visible in the Scanning Electron Microscopy (SEM) images in Figure 2a. The treatment also increased the oxygen content from 3 to 7 %, thereby improving the wettability. Xu *et al.*[39] thermally treated a pre-oxidised polyacrylonitrile (PAN) felt enclosed in a quartz vial at 1300 °C for 6 h to increase the surface area, then quickly immersed the capsule in liquid nitrogen and crushed it. This quenches the electrode, forming aligned micro-cracks in the fibre surface, noticeable in Figure 2b, increasing the surface area enhancing the transport of electrolyte to the electrode surface. The resulting electrode is further treated at 2200 °C and immersed in a sulphur-based solution to introduce sulphur functional groups. This method, which is still far from being industrially viable, showed an impressive increase in current density, reaching 500 mA cm^{-2} with an energy efficiency of $>$81 %. However, the defects generated by this method cannot be controlled and their role in this work are not explained. Defects might be crucial for

Table 1. Electrochemical performance of defective carbon electrodes for VFB at different experimental conditions.

Preparation method	Current Density [mA cm^{-2}]	Energy Efficiency [%]	Membrane	Cell Area [cm^2]	ref.
Thermal	400	81	Nafion 212	4	[38]
S-doped	500	81	Perfluorosuplhonic 25 μm		[39]
Plasma	100	84,5	Nafion 212	4	[42]
Plasma	160	77,5	Nafion 212	25	[45]
Chemical	250	72	Nafion 115	4	[46]
Chemical	150	72	Nafion 117	16	[19]
Graphene added	100	86	Nafion 212	13,5	[58]
Graphene added	100	87	Nafion 212	13,5	[57]
Nanosheets added/ N-doping	200	84	Nafion 212	9	[60]
CNT added	200	80	N/A	50	[62]
MFC	200	75	Nafion 115	4	[51]
Electrospinning	25	68	FAP 450	4	[66]
Electrospinning	200	80	Nafion 212	4	[68]
Chemical	200	80	Nafion 212	2,55	[52]

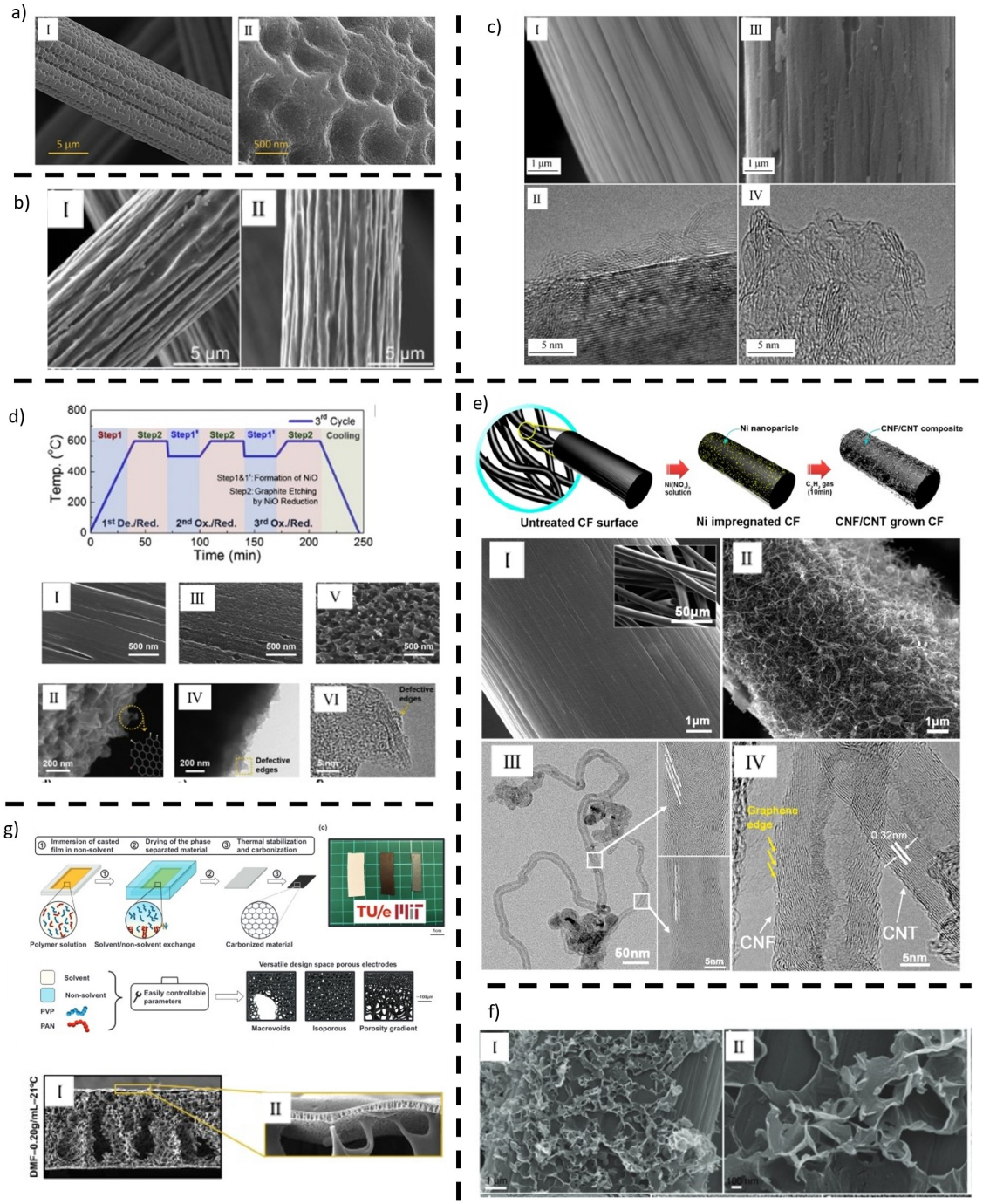

Figure 2. SEM, TEM images of morphology and processes scheme for manufacturing and engineering of electrodes for vanadium flow batteries. (a) SEM images at different magnification on morphology of the multiscale CF. Reprinted with permission from ref. [38] Copyright (2020) Elsevier. (b) SEM images at different magnification on morphology of the quench and crack electrode. Reprinted with permission from ref. [39] Copyright (2021) Elsevier. (c) SEM (I–III) and TEM (II–IV) images of plasma etched carbon fibre. Reprinted with permission from ref. [42] Copyright (2022) Springer. (d) Chemical etching cycles scheme, SEM (I–III–V) and TEM (II–IV–VI) images of the chemical etched carbon fibres. Reprinted with permission from ref. [19] Copyright (2016) Elsevier. (e) Fabrication scheme, SEM (I–II) and TEM (III–IV) images of CF coated with Carbon Nanofibres/Carbon Nanotubes. Reprinted with permission from ref. [50] Copyright (2013) ACS. (f) SEM images at different magnification of CF fibre coating with MFC. Reprinted with permission from ref. [51] Copyright (2022) Wiley. (g) process scheme and SEM images (I–II) at different magnification of novel gradient porous electrodes. Reprinted with permission from ref. [52] Copyright (2022) Elsevier.

efficient functionalisation of the surface, showing that they are reactive points for the introduction of heteroatoms.

Plasma treatment is another method to modify the structure of graphite fibres chemically and morphologically. This is achieved by the bombardment of the carbon surface with high energy ions and electrons that results in the formation of radicals and in the heating of the substrate leading to the etching of the surface morphology and chemistry modification.

In this way, Xu *et al.*[42] used an argon plasma to treat CF to introduce a large number of edge defects (Figure 2c). The higher content of defects in the structure is evident from Transmission Electron Microscopy (TEM) images, X-ray Photoelectron Spectroscopy (XPS) and Raman spectroscopy. Compared to pristine CF, the argon treated exhibited a slightly lower charge transfer resistance for the vanadium redox reaction. When the treated electrode is used as both anode and cathode, the performance exceeds that of the untreated CF by 6% at a current density of 100 mA cm^{-2}, which is ascribed to the presence of more defective sites. Moreover, the electrode also showed remarkable stability over 1000 charge-discharge cycles. In another study, Lin *et al.*[45] treated CF using an atmospheric plasma jet. Following the treatment, the felt was exposed to air for a few minutes, allowing the radicals formed to transform into OFGs. The roughness, attributed to the bombardment of accelerated heavy plasma species from the plasma jet, is believed to be beneficial for the VFB performance. These modifications led to significant improvements in the electrochemical performance. Hammer *et al.*,[53] adopting a similar setup, studied the effect of different working gases and time of exposure on the surface morphology. Results suggest that morphology modification, *i.e.*, roughness and surface area, do not depend on the working gas but on the exposure time. However, no information on the introduction of heteroatoms is reported using different working gases and no charge/discharge cycles were performed.

Chemical treatment can introduce defects and in particular functionalities on the carbon surface. Wu *et al.*[46] modified the surface of GF with a stream of nitric acid at high temperature to introduce OFGs. The oxidation reaction by nitric acid vapour occurs preferentially at the surface of the amorphous carbon and at defect sites. The removal of the inactive amorphous carbon contributes to the introduction of graphite edge sites and basal planes, which increase the double layer capacitance and improve the electrochemical activity, demonstrated by an energy efficiency of ~72% at a current density of 250 mA cm^{-2}. Although this process increases the defect density, there is no clear indication of the active participation of defects in the reaction kinetics in this work. Park *et al.*[19] deeply carved the surface of a CF by covering the surface with a coating of $Ni(NiO_3)_2$ and performing thermal treatments cycles (Figure 2d). More cycles resulted in a rougher surface with abundant defects. The etched surface exhibited a higher surface area and more edges, both beneficial for the electrochemistry. The resultant electrode showed improved energy efficiency (72%) and discharge capacity (10 Ah L^{-1}) at a current density of 150 mA cm^{-2}, which is doubled compared to the untreated one. Moreover, the edge site graphene structure was stable in acidic electrolytes for over 200 cycles at 100 mA cm^{-2}.

In general, subtractive methods for VFB electrode modification eliminate the possibility of fine defect finishing and focus mainly on increasing functional groups and surface roughness, which is found to be beneficial for the electrode performance. Methods need to be established to decouple the morphological changes and the functionalisation to clearly be able to attribute changes in the electrochemical properties to either one or the other.

2.1.2. Additive methods

In additive processes, new materials are applied to the fibre surface. These materials can be heteroatoms (metals or non-metals),[38,54–56] graphene,[57,58] carbon dots,[59] carbon nanosphere,[60,61] carbon nanotubes (CNT),[50,62,63] reduced graphene oxide,[63,64] or other carbon.[51,65] The surface area and defect concentration play a significant role in the final performance of the electrode. Although this technique is applied by various research groups, only a few of them focus on the development of high defect carbon coating. Long *et al.*[58] coated the surface of CF with a graphene layer deposited *via* chemical vapour deposition. The resulting electrode exhibited higher specific surface area (105 m^2 g^{-1}), defect density, oxygen concentration and thus catalytic activity. The results of charge/discharge cycles showed an energy efficiency $>$86% at a current density of 100 mA cm^{-2}. They attributed the higher catalytic activity to the synergistic effect of defects and high surface area. In subsequent studies by the same group,[57] defect density of the coated material was further increased *via* argon plasma treatment at room temperature. The modified electrode enhanced the catalytic activity, especially at the positive electrode, resulting in an energy efficiency of $>$87% at a current density of 100 mA cm^{-2}. This gain was mainly ascribed to the presence of oxygen in the defect sites, which changes the electronic structure of the graphene layers, increasing the electronic conductivity, as shown by DFT analysis.

Another simple but effective method to deposit carbon nanostructures on CF was performed by Huang *et al.*,[60] who synthesised a mixture of carbon microspheres and N-doped carbon nanosheets with moderate defects by hydrothermal treatment of guanosine. The synergy of these two elements enables the production of a coating material with a large surface area and catalytic activity. The mixture is applied to GF through long heat treatment in an autoclave followed by carbonisation at 1000 °C. The resulting electrode showed remarkable performance, reaching a current density of 200 mA cm^{-2} with an energy efficiency of about 84%. Another method for a fine dispersion of particles onto carbon fibres was proposed by Tai *et al.*,[62] dispersing CNTs into a solution of deionised water, ethanol and sodium dodecylbenzene sulfonate by stirring and sonicating the solution bath. The resulting solution was successively dropped into both side of CF and heated. The drop casted electrode showed a sharp Raman peak around 2700 cm^{-1}, typically present in CNTs, graphene and other carbon allotropes with large layer interspace, attributed to defectiveness among graphene layers. The electrochemical performance of the produced electrode was higher than pristine CF, with an energy efficiency close to 80% at 200 mA cm^{-2}.

In another study, Park *et al.*[50] explored the synthesis and application of a composite catalyst made of carbon nanofibres (CNF) and CNTs on CF. The CNF/CNT composite was synthesised

using C_2H_2 gas at different temperatures (500 to 800 °C). The growth process (Figure 2e) was facilitated by Ni nanoparticle seeds, and the temperature control led to the formation of unique morphologies. The formation of large edge plane defects in CNF and basal planes in CNT walls were observed by TEM (Figure 2e). The CNF/CNT electrodes were tested in a 5 cm^2 cell area showing an increased discharge capacity of 25 $Ah L^{-1}$, 64% higher compared to the untreated CF. The authors ascribed the performance gain to the surface defect sites of exposed edge planes in CNF and to the fast electron transfer rate of the in-plane side wall of the CNTs. In a recent study done by Deng and co-workers,[51] a novel manufacturing method was developed to create a multidimensional frame carbon (MFC) structure with coexistent 0D, 2D, and 3D structures (Figure 2f). This unique composition was achieved through the recrystallisation of sodium citrate molecules on carbon fibre. The process led to the formation of nanoparticles, nano-sheets, and interlaced carbon nanosheets, rich in edge defects and mainly composed of sp^2 carbon. Electrochemically, the MFC material demonstrated superior performance reaching a maximum current density of 500 $mA cm^{-2}$ (energy efficiency close to 55%) and a stable current density of 200 $mA cm^{-2}$ at 75% energy efficiency for over 400 cycles. Furthermore, the paper presents a DFT study to identify the reaction sites on the MFC material in both positive and negative electrolytes. The study found that edge carbon atoms act as the most reactive site.

Additive processes can provide good tunability of the properties of the resulting electrode, but their application is hindered by the high manufacturing cost and low production rate.

2.1.3. Novel carbon-based mesoporous electrodes

Electrospinning is a nanofibre fabrication method that is gaining popularity as the preferred fabrication method for mesoporous carbon electrodes. Electrospun nanofibres offer several advantages over conventional CF, including greater specific surface area, better control of pore size and distribution, and improved mechanical properties. Electrospinning novel carbon fibre materials could enable the creation of defects in the manufacturing process, eliminating the need for deposition of functional materials and surface treatments. One method explored is the incorporation of functional materials during electrospinning.[66–68] As an example, Maleki *et al.*[62] reported on the incorporation of carbon black into PAN-based nanofibres, resulting in fibres with increased mean diameter and rough surface. The study revealed that the loaded mat exhibited a significantly higher specific surface area compared to commercial CF. The incorporation of carbon black not only increased the fibre diameter but also contributed to the large surface area due to its micro-porosity and superior surface roughness. Moreover, the resulting electrode has a high defect concentration as determined by Raman spectroscopy. However, since the performance in a battery was lower than the commercial CF (energy efficiency of 68% versus 69% at 25 $mA cm^{-2}$), the study identified challenges related to mass transport limitation and inter-fibre distances, suggesting future optimisation. Optimisation performed by the same author[68] focused on the incorporation of polyaniline and carbon black into PAN and polyacrylic acid based nanofibres, aiming to enhance the electrochemical activity towards the VO^{2+}/VO_2^{+} redox reactions. The higher presence of surface defects and amorphous carbon translated to a higher catalytic activity for the vanadium redox reactions measured by cyclic voltammetry. However, no full cell charge-discharge cycles were performed with this electrode material, so no indication on performance versus the commercial CF is given.

The addition of sacrificial materials during electrospinning that can be removed during carbonisation is another strategy used in electrospinning of carbon electrodes. Sun *et al.*[69] studied carbon mesoporous electrodes produced by electrospinning of PAN and polystyrene, followed by thermal treatment at 250 °C for 2 h and annealing in N_2 environment at 1100 °C for 1 h. During the thermal annealing, the polystyrene completely decomposed resulting in cavities inside the fibres. The resulting carbon mat showed an energy efficiency of over 80% at 200 $mA cm^{-2}$. The authors correlate the electrochemical performance to a higher surface area and increased mass transport over many defects detected by Raman spectroscopy. Zhang *et al.*[70] prepared a mesoporous CF by electrospinning a solution of poly(methyl methacrylate) and PAN dissolved in N,N-dimethyl formaldehyde. The obtained felt was successively pre-oxidised at 280 °C for 1 h and carbonised at 1000 °C for 2 h. Due to the poor compatibility of PAN with poly(methyl methacrylate), the latter is removed during annealing, resulting in the formation of voids and porous nanochannels inside the fibres. The resulting felt exhibited higher electrochemical double layer capacitance and energy efficiency, along with remarkable long-term cycling stability, which was attributed to the increased surface area, higher defect density, and more OFGs.

Sacrificial agents were also adopted in other techniques different from electrospinning. For instance, Wan *et al.*[71] studied a polymer solution of Poly(vinylpyrrolidone) and PAN at different ratios in a non-solvent induced phase separation to synthesise a tuneable porous electrode (Figure 2g). The process is promising for an industrial process and allows the fine tuning of the porosity which is beneficial for the electrolyte transport in the electrode. After a post-carbonisation treatment, the electrodes showed the same defectivity of CP. Due to the presence of nitrogen in PAN, the resulting electrode contained nitrogen groups, which were beneficial for the vanadium reaction kinetics. In a later work by the same group[52] the effects of solvent and non-solvent chemistry, temperature and polymer concentration were optimised. The author focused primarily on maximising the electrolyte mass transport inside the electrode. The resulting electrode morphology (Figure 2g) is characterised by a gradient porosity. Raman spectroscopy of the produced electrode indicated an overall defectiveness of the carbon structure. A small VFB cell mounted with the gradient porous electrode had a peak power of 1 $W cm^{-2}$ and

charge-discharge cycles showed an energy efficiency of 80% at 200 mA cm^{-2}.

Novel methods for electrode fabrication can achieve incredible results thanks to the fine tuning of all the properties of the formed fibre. However, the porosity of the electrode is generally one order of magnitude lower than that of the commercial electrode. This can lead to an increase in the pressure drop in VFBs, resulting in higher pumping losses which is why most of the work on novel techniques for electrode fabrication focus their attention on porosity more than on defectiveness.

2.2. Electrodes in Sodium Ion Batteries

SIBs have received considerable attention in recent years due to their potential as a cost-effective and sustainable alternative to lithium-ion batteries. HC is a promising anode material for SIBs due to its high reversible specific capacity and low voltage plateau. HCs are traditionally synthesised by pyrolysis under an inert atmosphere,[72] with prior or post-treatments to purify the carbonaceous materials, or by sintering of carbon precursor in an inert atmosphere. The synthesis conditions, such as the precursor type and temperature, can significantly impact the characteristics of the resulting HC. The precursor materials used to develop HC can be grouped into three main categories: synthetic polymers,[73] biopolymers, and raw biomass.[74,75] The latter are gaining more interest world-wide due to their low-cost and high defect density. Chen *et al.*[14] studied the performance of a starch-derived HC by yeast fermentation of corn. The fermentation process drastically changed the structure by increasing internal closed micropores, layer spacing and disorder. From the TEM images in Figure 3a, the resulting structure has a turbostratic character consisting of multiple defects and highly disordered graphitic planes. The electrochemical properties of the fermented corn starch electrode were tested in a half-cell. The charge/discharge profile showed a reversible capacity of 335 mA h g^{-1} and an ICE $>$87%, with an

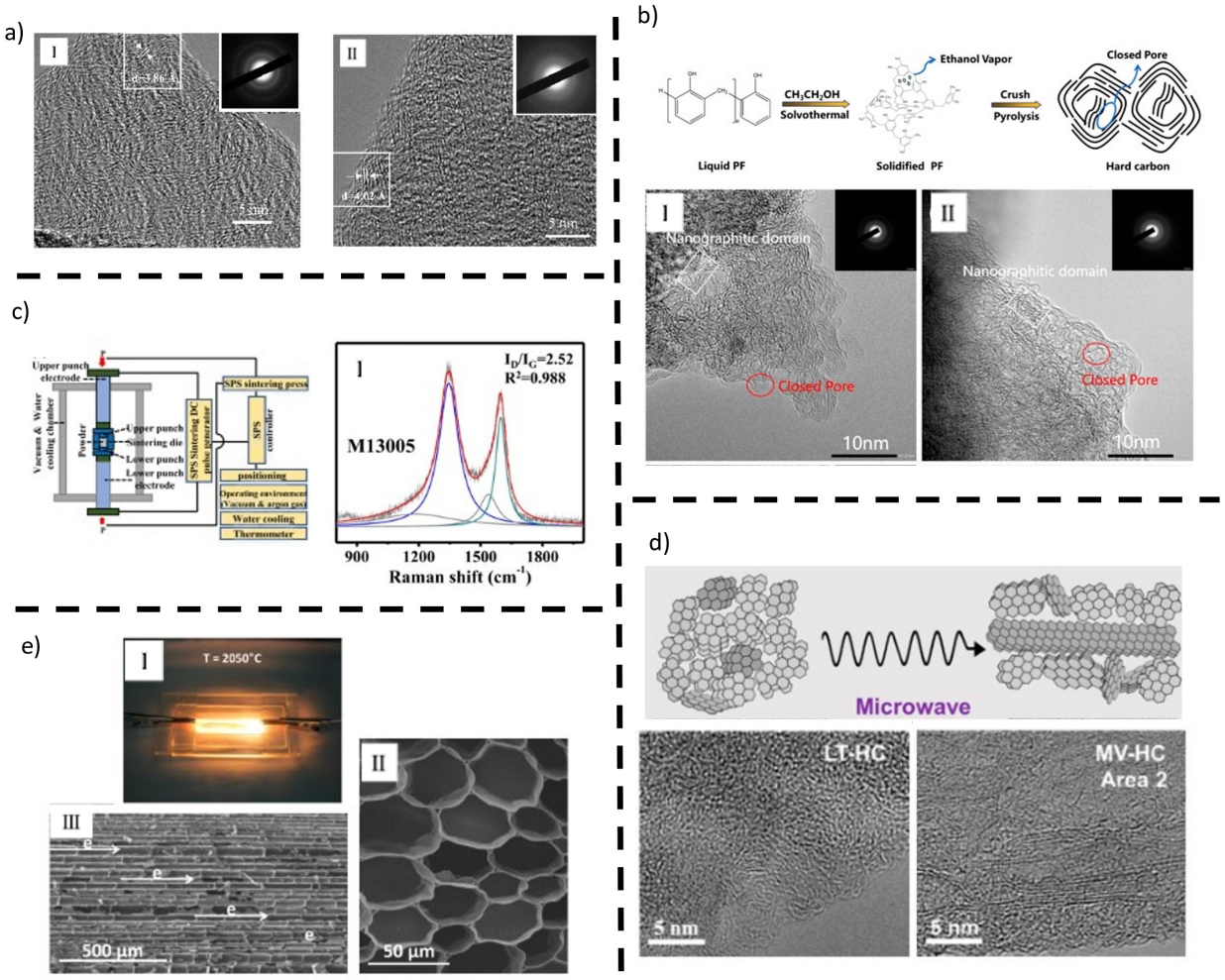

Figure 3. TEM images, process scheme and SEM images for manufacturing and microengineering of electrodes for SIB. (a) TEM images of HC produced from fermentation of starch. Reprinted with permission from ref. [14] Copyright (2023) Elsevier. (b) process scheme and TEM images (I–II) of closed pore in HC produced by ethanol solvothermal and pyrolysis. Reprinted with permission from ref. [73] Copyright (2019) ACS. (c) process scheme of SPS and Raman spectra of HC. Reprinted with permission from ref.,[76] used under Creative Commons CC-BY licence. (d) sketch of microwave process and TEM images of HC produced by low temperature pyrolysis (I) and microwave heating (II). Reprinted with permission from ref. [16] Copyright (2018) ACS. (e) picture of the joule heating and SEM images of the longitudinal (I) and cross section (II) carbonised grass. Reprinted with permission from ref. [77] Copyright (2017) ACS.

increase of 82 mAh g^{-1} compared to the unfermented electrode. The increase in reversible capacitance was attributed to defects and OFGs that contributed to the formation of sodiophilic sites on the HC surface and enhanced the capacitive storage behaviour of sodium. Meng *et al.*[73] developed a green chemical regulation approach to tune the microstructure of phenol formaldehyde resin-derived HC anodes adding ethanol and performing a solvothermal treatment of 2 h prior to the pyrolysis (Figure 3b). By adjusting the content of ethanol, closed pores are well controlled. The full cell exhibited a high reversible capacity of 413 mAh g^{-1}, a high ICE of 83%, and a high energy density of approximately 300 Wh kg^{-1} at 0.1 C. High-resolution TEM highlights a turbostratic graphitic microstructure where the disordered and curved graphene sheets are cross-linked to form closed pores ~2 nm.

Wang *et al.*[75] systematically studied the effects of carbonisation time on mangosteen shells. As depicted by TEM and Raman spectra, the microstructure of the resulting HC is deeply affected by the temperature and time of carbonisation. Optimising temperature and time, the authors were able to produce HC with 320 mAh g^{-1} at a current density of 20 mA g^{-1} and a capacity retention of 98% after 100 cycles and an ICE of 83%. However, traditional methods are generally energy-intensive and time consuming since they require a slow heating rate and a high peak temperature to graphitise the precursor.

2.2.1. Novel fabrication methods for Hard Carbon anodes

New fabrication methods for defective HC aim to decrease the energy consumption while maintaining a high production rate. We can find fast sintering processes,[76] microwave[77] and joule heating,[16] and laser annealing of carbon precursors.[78] The spark plasma sintering process developed by Zhen *et al.*[76] allows for rapid fabrication of HCs from different carbon precursors at an ultrafast heating rate (300–500 °C min^{-1}) in $<$1 min. The technology is a field-assisted sintering process that combines plasma activation, hot pressing, and resistance heating (Figure 3c). Typically, the powder sample is put into a circular graphite tank, and a graphite plate is used as a substrate. Even though the authors state that the HCs prepared in such manner have significantly fewer defects, lower porosity, and a lower oxygen content than those pyrolysed in traditional sintering ways, the intensity ratio in the Raman spectra (Figure 3c) is too high to define undefective carbon. The prepared HC exhibited an improved ICE (88.9%) and a larger reversible capacity (~300 mAh g^{-1}) compared to anode materials derived by pyrolysis.

A significant breakthrough was the preparation of highly defective HC through a novel microwave treatment process.[16] This method involved the pyrolysis of cellulose at 650 °C to obtain carbon, followed by microwave treatment for 6 s. The result was an increase in the reversible capacity of the HC from 204 to 308 mAh g^{-1}, a performance that surpassed that of HC annealed at 1100 °C for 7 h. The microwave treatment not only proved to be energy-efficient but also retained a high extent of the structural vacancies in HC, which can be seen in the TEM images in Figure 3d. In addition to a higher slope capacity, it also exhibited a low-potential plateau capacity of ~60% of its total capacity. However, due to its proximity to the sodium plating potential, the low potential plateau raises concerns about dendrite formation. Therefore, a predominantly defective HC may potentially increase the overall capacity and address safety concerns. Zhang and co-workers[77] carbonised switchgrass by the adoption of a joule heater (Figure 3e). The biomass precursor was first carbonised in a tubular furnace at 1000 °C in an argon environment, followed by pyrolysis at 2050 °C. The grass scaffold is retained after the thermal treatment, resulting in a mesoporous carbon electrode with roughly 30 m^2 g^{-1} surface area and structured hollows, visible in the SEM images (Figure 3e). With respect to the grass carbonised at 1000 °C, the 2050 °C sample exhibited sharper signals in the X-ray diffraction pattern, suggesting a higher crystallinity at an almost unchanged defectiveness according to Raman spectroscopy. The fast-carbonised electrode was tested for over 800 cycles at 50 mA g^{-1} with a stable discharge capacity of 200 mAh g^{-1}.

The exploration and development of SIBs with HC as an anode material have opened new horizons in the field of energy storage. The synthesis and treatment methods, ranging from traditional pyrolysis to innovative techniques like microwave treatment and spark plasma sintering, have shown significant impacts on the structural and electrochemical properties of HC. The emergence of novel fabrication methods that reduce energy consumption while maintaining high production rates signifies a promising direction for future research. The insights gained from these studies contribute to a deeper understanding of the complex relationship between the structural characteristics of HC and its electrochemical behaviour, paving the way for the optimisation of SIBs.

3. Intrinsic defects and heteroatom doping of hard carbon for sodium-ion batteries

3.1. Hard Carbon – a unique member of the carbon family

The structurally well-defined allotropes of the carbon family offer benefits for a wide range of applications. Graphite for example demonstrates electrical conductivity and has established itself an indispensable component in lithium-ion battery systems. Although lithium intercalation into graphite has proven to be a successful method for energy storage, this approach cannot be directly applied to its heavier homologue sodium. Unfavourable interlayer spacing of the individual graphene sheets in graphite and the positive intercalation enthalpy of sodium render the performance of graphite anodes in SIBs insufficient for energy storage.[79] Graphite as anode material underperforms in SIBs with inferior reversible capacities of 35 mAh g^{-1} (corresponding to a NaC_{64} stoichiometry) compared to 372 mAh g^{-1} (corresponding to LiC_6) in lithium-based batteries.[80]

The pioneering work of Stevens and Dahn[81] in 2000 paved the way for the growing interest in non-graphitizable carbons

as a potential anode material for SIBs over the past decade. Their proposed model describes the turbostratic structure of HC as a 'house of cards' where the cards are considered small aromatic fragments orientated in a random fashion. The resulting nanoscale porosity and layered structure provides storage sites for sodium ions along with defects and heteroatoms enabling reversible capacities beyond 300 mAh g^{-1}.

Contrary to the ordered stacking of graphene sheets in graphite, the planes in HC are curved, misaligned and randomly orientated (Figure 4k).[13,17] On a atomistic level, the individual sheets consist of sp^2 hybridised carbon hexagons in a honeycomb structure featuring defects such as vacancies, dangling bonds at the edges, five or seven membered rings and bridging carbon atoms (Figure 4a–j).[17,82] The lattice experiences strain due to these defects, resulting in the curvature and increased interlayer distance between the graphene sheets. The parameters, which can be used for quantification are the curvature of the graphene fringes, the length (L_a) of the graphene, the number of graphene layers and their interlayer distance (d_{002}).[83,84] HRTEM studies of HC from petroleum coke corroborate the curvature and show that the fringe length in HCs can be smaller than 20 Å. The ordering degree of the fringes is low with only 25 % of the fringes stacked and a considerably low stacking number of 2.92 sheets per stack (Figure 4m).[83]

To investigate the impact of curvature in individual graphene sheets, Song *et al.*[85] employed chemical vapour deposition of methanol on HC, allowing the growth of intricately curled graphene sheets (Figure 4n). According to their studies, the graphene sheets preferentially nucleate at defect-sites and grow in a longitudinal-oriented way. Thereby, they are developing a curved structure when they mismatch (Figure 4n). Their findings revealed that the presence of curled graphene sheets on the surface effectively shields defects on the HC surface, while concurrently creating additional active sites for reversible Na^+ storage through the formation of closed micropores. The defect-shielded surface delivered a high ICE of 89.3 % and the additionally formed micro-porosity allows a high reversible capacity of 358 mAh g^{-1} at a current density of 30 mA g^{-1}.

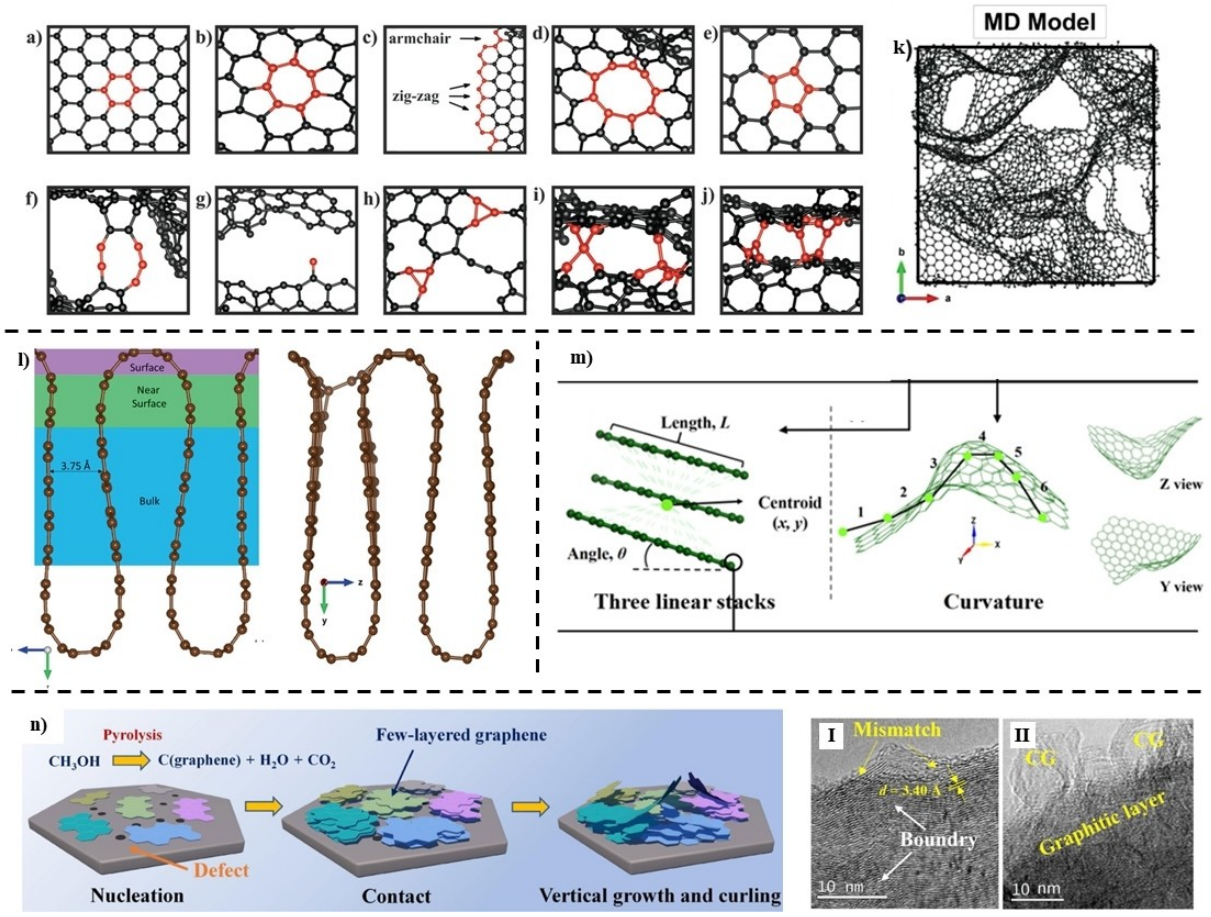

Figure 4. (a–j) Schematic representations of different structures present in HCs (a: hexagonal rings, b: 7-membered rings, c: zigzag and armchair edges, e: 5-membered rings, f: bridging methylene moieties, g: methyl groups, h: 3-membered rings, i: sp^3 bridging bonds, j: sp^2 bridging bonds). (k) Molecular dynamics simulation of HC showing the curvature. Reprinted with permission from ref. [17] Copyright (2022) Wiley. (l) Schematic representation of the different regions in the model (blue: bulk-like, green: near surface, purple: surface) and the bridging carbon after introduction of a defect. Reprinted with permission from ref. [13], used under Creative Commons CC-BY licence. (m) parallel stacking and curvature of the fringes in HC. Reprinted with permission from ref. [83] Copyright (2022) IOP. (n) Schematic illustration of the growth of curled graphene sheets on HC surfaces and HRTEM images of I) the mismatch and II) growth of curled graphene sheets. Reprinted with permission from ref. [85], Copyright (2023) Springer.

In a computational study, Olsson *et al.*[13] systematically investigated the effect of vacancies, oxygen and nitrogen substitution in a curved graphene sheet consisting of 800 carbon atoms (Figure 4l). Selected carbon atoms in the plane were removed to introduce defects and assess their influence. By performing energy calculations for the defect formation, it was possible to evaluate the concentration of defects. It was observed that vacancies are more likely to occur near the surface rather than in the bulk, and crosslinking can take place near the surface (Figure 4l). The vacancy leads to a local distortion of the lattice resulting in a higher interlayer spacing, thus rendering sodium adsorption energetically favourable.

The inherent porosity of HCs due to the release of gas molecules during pyrolysis poses an additional significant factor for sodium storage. Two distinct forms of porosity are usually considered to describe the texture of HCs (Figure 5a). Open pores can be accessed by the electrolyte and contribute to the surface area, whereas closed pores are present inside the particles and can support sodium storage. According to the study conducted by Beda *et al.*,[86] an increase in the carbonisation temperature leads to a gradual reduction in the specific surface area and an increase in the amount of micropores with a diameter smaller than 2 nm (Figure 5b). Furthermore, the adsorption gas plays a key role in the characterisation method, as CO_2 can assess pores which are too narrow for N_2. This allows the quantification of micropores with diameters smaller than 0.7 nm (Figure 5c). Besides the pyrolysis temperature, the heating rate is another crucial parameter to be responsible for the pore evolution and structure of the HCs. Lu *et al.*[87] demonstrated that surface area and micropore volume can be correlated to the heating rate of the precursor. A slower temperature ramp encourages the development of a closed pore structure, as it provides sufficient time for gas molecules to escape from the particle. Consequently, the surface area was reduced from 34 $m^2 g^{-1}$ at a heating rate of 5 $K min^{-1}$ to 1.72 $m^2 g^{-1}$ at a decreased heating rate of 0.5 $K min^{-1}$. The low surface area and small porosity minimises the electrolyte decomposition and the formation of a solid electrolyte interface (SEI) leading to a high ICE (Figure 5c). By employing *ex situ* NMR techniques, evidence of metallic clustering inside enclosed pores of HCs subjected to high-temperature pyrolysis was established.[88,89] The metallic character was evident from the prominent peak observed at 1135 ppm in the NMR spectra in Figure 5d. The high carbonisation temperature reduces defects and interlayer spacing while simultaneously closed pore volumes are increasing. In HCs carbonised at lower temperatures, sodium is predominantly stored at defect sites and functional groups. However, at higher carbonisation temperatures, the development of voluminous closed pores provides the potential for sodium cluster growth (Figure 5e).

3.2. The choice of the precursor – artificial or biomass derived

One of the defining characteristics of HC is their origin from precursors of both natural and synthetic sources. The pathways for synthesising HC can take multiple approaches. The top-down approach inherits the already established microstructures

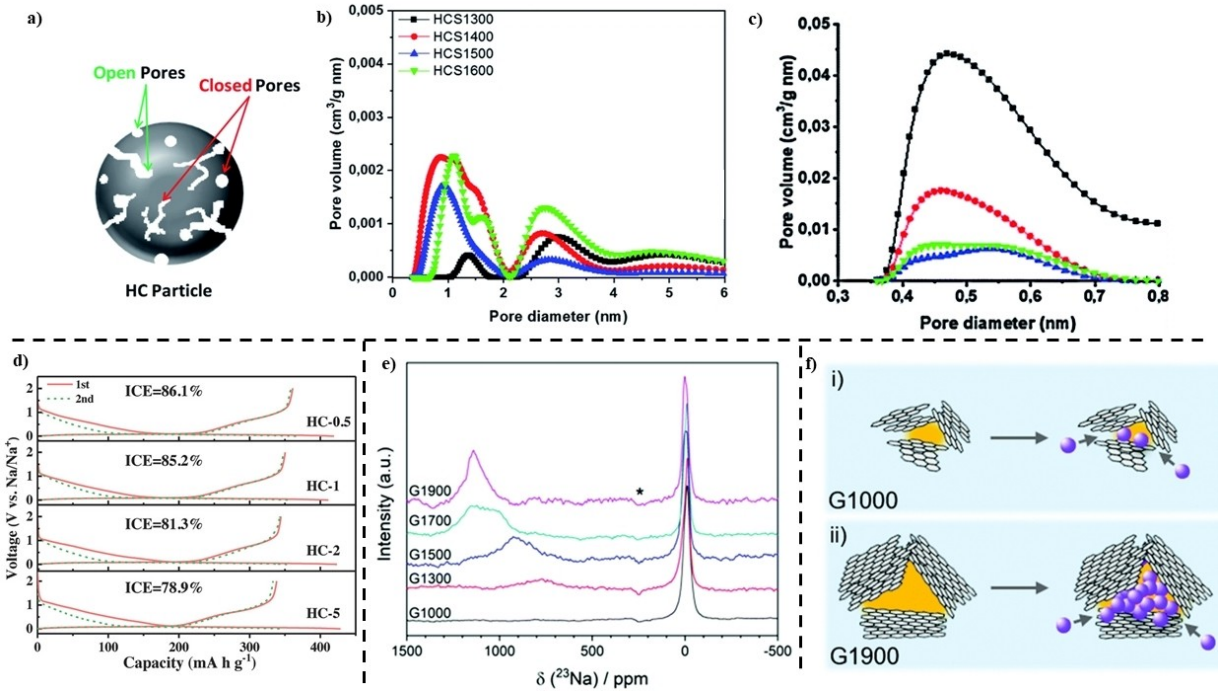

Figure 5. (a) Schematic illustration of a HC particle with its closed and open porosity. (b) Distribution of pore sizes by N_2 and CO_2 (inset). Reprinted with permission from ref. [86] Copyright (2021) RSC. (c) First and second cycle galvanostatic charge/discharge profiles of HCs pyrolysed at 1300 °C with different heating rates. Reprinted with permission from ref. [87] Copyright (2018) Wiley. (d) *Ex situ* ^{23}Na MAS NMR of HCs carbonised at different temperatures and after discharging to 5 mV; (e) Schematic illustration of sodium storage where no metallic sodium is detectable (i) and clustering in closed pores (ii). Reprinted with permission from ref.,[88] used under Creative Commons CC-BY licence.

from natural precursors (*e.g.*, inheriting the xylem vessels in leaves). HCs from biomass precursors like wood, wastes from agriculture or livestock often do not exhibit a defined chemical structure, as many environmental factors define the chemical composition of biomass. Due to the distinct electrochemical characteristics of each precursor, it can be demonstrated that HC from different tree species yield varying capacities ranging from 204 to 268 mAh g^{-1}.[90] Other biomass precursors from wastes like coconut or walnut shells deliver reversible capacities of ~207 to 293 mAh g^{-1}.[91] The use of biomass-derived chemically well-defined building moieties, such as carbohydrates, represents a good way to exclude environmental and seasonal factors. Different sugars like sucrose, glycogen or cellulose deliver reversible capacities ranging from 296 to 317 mAh g^{-1} with high ICEs of around 87 to 94%.[92]

The manifold available biomass precursors, treatments and pyrolysis temperatures render comparability throughout literature complicated.[93] On the other hand, the bottom-up approach involves synthetic polymers or well-defined natural polymers and subsequently subjecting them to pyrolysis. While this approach may seem less sustainable, it may be better suited for systematic studies as the carbon yield is higher and results are more consistent and reproducible. Resinous precursors such as phenolic, epoxy, melamine or resorcinol formaldehyde resins are commonly used.[94–96] Table 2 compares different synthetic and biomass-derived HCs regarding their oxygen content and electrochemical performance.

During pyrolysis, precursors undergo complex reactions that lead to the development of a highly disordered carbon structure. The pyrolysis processes can be divided into three stages: (i) the cleavage of heteroatoms (<1000 °C); (ii) the nucleation and growth of graphenic multilayer domains (1000 to 2000 °C) and (iii) the progressive graphitisation of the material (>2000 °C).[97] The boundaries between the stages, however, are not rigidly defined and can overlap depending on the precursors chemistry, allowing for concurrent progression of processes. Gomez-Martin *et al.*[98] observed a peak in the interplanar distance of olive-stone derived HC at 1400 °C with decreasing tendencies at even higher pyrolysis temperatures of up to 2000 °C. They attribute this behaviour to the growth of graphitic domains, a reduction in defect concentration and interlayer cross-linking.

There is an urgent need for a systematic approach to determine levels of oxygen functionalisation, intrinsic porosity, and graphitisation degree. Huang *et al.*[99] pyrolysed shaddock peels to obtain HC with a high number of surface C=O groups, which served as capacitive sodium storage sites and additionally improved reaction kinetics. A study by Chen *et al.*[100] employed buckwheat husks as a precursor to achieve a high degree of C=O functionalisation in their HC. Samples pyrolysed at 1100 °C delivered a high reversible capacity of 333 mAh g^{-1} at a current density of 50 mA g^{-1} after 400 cycles. The electrochemical performance was attributed to the natural pore structure and C=O groups. First-principle computational studies corroborate their findings, suggesting that C–O and C=O bonds have an influence on the adsorption capacity for sodium ions.

3.3. Heteroatom doping – a facile tuning method

Introduction of heteroatoms namely phosphorus, sulphur, nitrogen, and boron into the HC lattice can be utilised for tweaking of different characteristics, such as interlayer spacing, crystallite size, the SEI formation or electrochemical properties such as reversible capacities. Phosphorus and sulphur doped HC exhibits an increase in interlayer spacing and curvature in the

Table 2. Electrochemical performance of HCs derived from natural and synthetic precursors.

Precursor	Pyrolysis temperature	O-content [at%]	Electrochemical Performance [mAh g^{-1}]	ICE [%]	Electrolyte	Ref.
Walnut shells	1300 °C	3.4	293 at 50 mA g^{-1} after 100 cycles	66	1 M $NaPF_6$ diglyme	[91]
Coconut shells		8.5	270 at 50 mA g^{-1} after 100 cycles	63		
Corn silk		6.8	273 at 50 mA g^{-1} after 100 cycles	62		
Shaddock peel	600 °C	12	380 at 50 mA g^{-1} after 500 cycles	70	1 M $NaClO_4$ EC:DEC	[99]
Buckwheat husks	1100 °C	4.1	333 at 50 mA g^{-1} after 400 cycles	54	1 M $NaClO_4$ EC:DEC (+2 wt% FEC)	[100]
Resorcinol/phenolic resin	1100 °C	6.9	281 at 100 mA g^{-1} after 200 cycles	82	1 M $NaClO_4$ EC:DEC	[94]
Phenolic/formaldehyde resin	1100 °C	24.8	196.9 at 100 mA g^{-1} after 300 cycles	85	1 M $NaClO_4$ EC:DEC	[95]
Epoxy resin	1500 °C	3.8	235 at 100 mA g^{-1} After 200 cycles	81	1 M $NaPF_6$ EC:DMC	[96]

material due to their vastly elevated atom size when compared with carbon. Both characteristics lead to an enhanced diffusion of Na^+ between the graphene layers and an increased uptake inside the pores. Heteroatom doping can be achieved by various techniques, most commonly different oxyacids, such as H_3PO_4 or H_2SO_4, as doping agents. Alvin *et al.*[101] achieved phosphorus-doping by submersion of lignin in H_3PO_4 solution and ensuing carbonisation. The resulting HC displayed a capacity increase from 261 mAh g^{-1} to 319 mAh g^{-1} with a simultaneous increase of plateau contribution from 64 to 68% because of enlarged interlayer spacing from 3.74 Å to 3.87 Å. Similar behaviour was observed by Hong *et al.*[102] for sulphur-doped HCs carbonised using elemental sulphur and pitch as precursors. An enlargement in interlayer spacing to 4 Å was observable with a twofold increase in reversible capacity of 400 mAh g^{-1}. For sulphur it is frequently necessary to reduce the carbonisation temperature <650 °C due to the formation of SO_2 gas. This can lead to a reduced degree of heteroatoms which can only be partially overcome by shortening of the carbonisation time, increase of doping agent or by precursors with sulphur incorporated in the chemical structure.[103]

Contrary, nitrogen and boron doped HCs display no significant changes regarding curvature or interlayer spacing. Instead, the formation of defective sites on the graphene layers itself is promoted. Furthermore, sodium storage is boosted due to nitrogen's five and boron's three valence electrons, where additional sodium ions can be deposited. Wu *et al.*[104] achieved boron-doping by mixing of glucose and boric acid followed by subsequent carbonisation. The resulting doped HC showed only minor variations to the undoped in terms of crystallite size or interlayer spacing. Reversible capacities were improved from 168 mAh g^{-1} to 234 mAh g^{-1} for carbonisation at 1200 °C. The authors observed a significant increase in the plateau capacity, which they concluded to be caused by an increased number of intercalated sodium. Heteroatom doping with nitrogen is the most prevalent technique in literature due to the high prevalence of nitrogen in many precursors, especially waste products, or doping agents which greatly lowers cost and reduces complexity of the synthesis. Wang *et al.*[105] carbonised polyimide separators sourced from used lithium-ion batteries to collect HC with ~3 at% nitrogen and highly reversible capacities up to 190 mAh g^{-1} even after 100 charge-discharge cycles.

3.4. Hard carbon surfaces as a key to high initial coulombic efficiencies

Maximised charge retention during the initial cycle plays a pivotal role in enhancing the energy density in batteries. The reservoir of cyclable sodium in full cells is mostly dictated by the active material of the cathode and the formation of the SEI is considered the most important factor of charge-loss. The SEI acts as a passivating layer on the surface, hindering the progressive decomposition of the electrolyte, while simultaneously allowing the diffusion of sodium ions. The presence of defects and functional groups on the surface of the HC is of great importance, as they have the potential to act as nucleation sites. Temperature-programmed desorption mass spectrometry can assess the degree of oxygen functionalisation. Acidic functional groups mainly decompose into CO_2 while basic or neutral groups yield CO.[106] Ghimbeu *et al.*[107] probed the oxygen surface functionalisation of HC derived from cellulose which was pyrolysed at different temperatures. Figure 6a illustrates in the desorption profiles that between 400 and 950 °C, mainly the basic and neutral groups such as phenols, ethers and quinones decompose. Between 200 and 750 °C a much lower evolution of CO_2 is recorded, suggesting that carboxyl groups and anhydride groups are less present on the surface. Additionally, the release of water molecules was detected between 100 and 600 °C, which was ascribed to the release of physisorbed water in the pores at lower and chemisorbed water at higher temperatures. It is further proposed that oxygen functional groups (OFGs) are presumably present on defect sites, when the HC is exposed to air after pyrolysis in an inert atmosphere. HC samples were treated with a concentrated nitric acid to introduce more OFGs, which were then reduced by annealing in H_2 atmosphere at 900 °C. The ICE dropped from 82.7 to 55.9% after oxidation and decreased further to 48.2% when the acid treated sample was annealed in H_2 atmosphere (Figure 6b).

Computational studies suggest that a possible decomposition site of ethylene carbonate (an integral part in many electrolytes for SIBs) is located at regions with a high concentration of oxygen-containing defects.[108] While the breakdown product C_2H_4 shows almost no interaction with defects, CO_3^{2-} can be further broken down to CO_2 and an oxygen-functionalised defect site (Figure 6d). Density Functional Theory (DFT) studies further suggest, that sodium adsorption is more favourable at a functionalised basal plane than edge site and reaction of OFGs with sodium leads to the formation of inorganic compounds.[109] Shen *et al.*[110] employed a low temperature oxygen plasma treatment to introduce OFGs on HC. They ascribed the increased plateau capacity of oxygen plasma-treated samples with the higher degree of graphitisation and the higher sloping capacity with the selective introduction of C=O groups. Furthermore, the ICE was increased from 60.6 to 80.9%. Their proposed interaction of sodium with C=O surface groups is the reversible reaction $Na^+ + -C{=}O + e^- \rightarrow Na{-}O{-}C-$, which is also proposed by other studies.[111]

A correlation between the surface functionalisation of HCs with OFGs and defects was also reported by Luo *et al.*[112] By mixing the argon gas during pyrolysis with different molecule vapours (cyclohexane or ethanol), an *in situ* engineering of the HC surface was achieved. Decomposition of the molecules in the carrier gas to highly reactive carbon species can cure defects and react with the functional groups on the surface of the HC. XPS analysis revealed that the oxygen content was decreased from ~5 to ~1 at%, while the ratio of sp^2 to sp^3 carbon increased from ~9 to 15. Re-introduction of OFGs by chemical treatment with a mixture of nitric and hydrochloric acid increased the oxygen content to 16 at% at a decreasing sp^2 to sp^3 ratio to ~5. Treatment of the HC with oxidising acids however led to an ICE of ~30%, which is in accordance with other reported literature (Figure 6c).[107,113] Contrasting, it is also

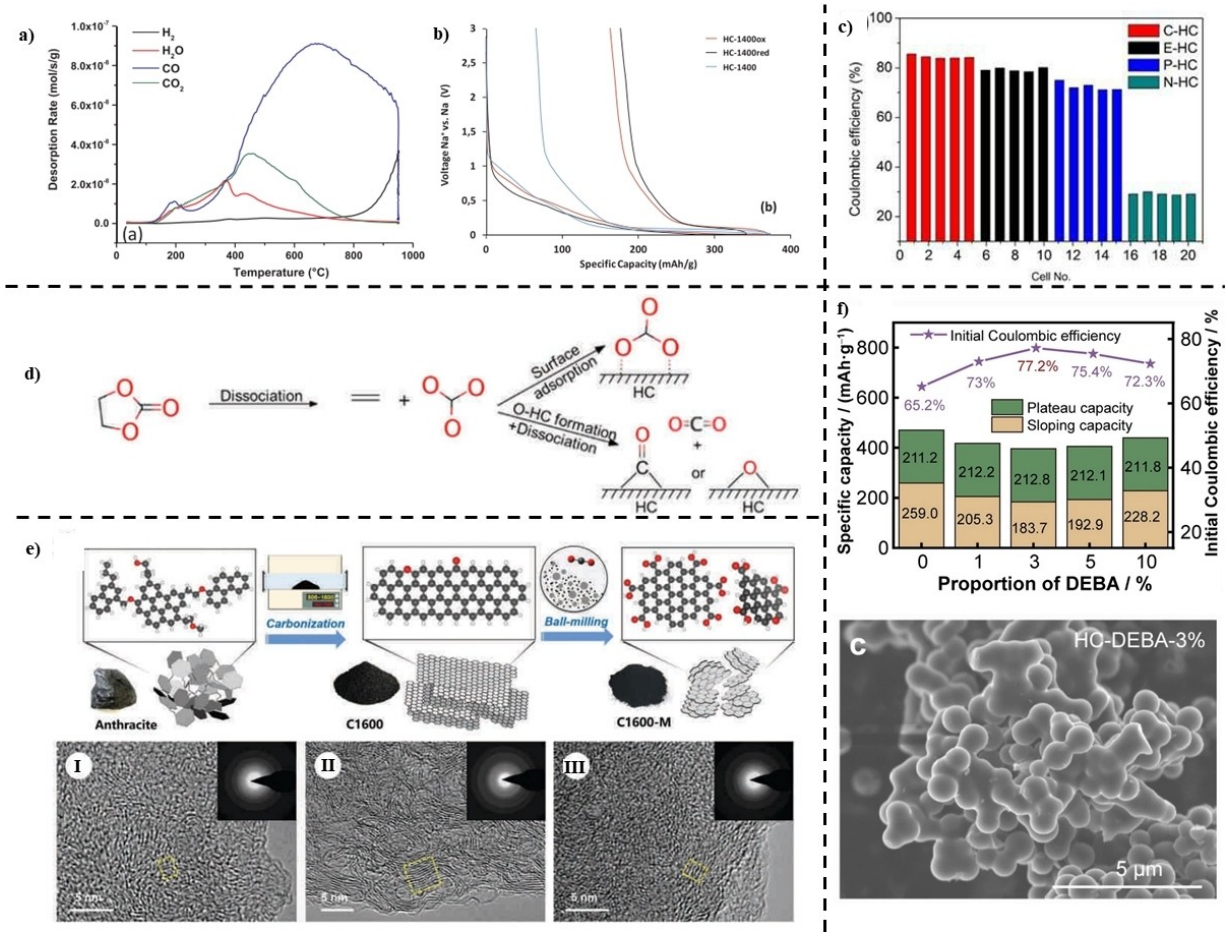

Figure 6. (a) TPD-MS curves of cellulose during pyrolysis; (b) first cycle of HC cycled at C/10 with 1 M $NaPF_6$ in EC:DMC (1:1). Reprinted with permission from ref. [107]. Copyright (2018) Elsevier. (c) Comparison of ICEs from HCs pyrolysed in cyclohexane (red) or ethanol (black) vapours, in argon environment (blue), and acid treated (green). Reprinted with permission from ref. [112] Copyright (2019) Elsevier. (d) possible reaction mechanism of carbonate with defects on the surface. Reprinted with permission from ref. [109] Copyright (2021) Elsevier. (e) mechano-chemical modification of anthracite derived HC by ball-milling. Reprinted with permission from ref. [115] Copyright (2020) Wiley. (f) Initial coulombic efficiencies of a DEBA functionalised HC (upper panel) and SEM image of DEBA coated HC. Reprinted with permission from ref. [116] Copyright (2022) Springer.

reported that treatment of HC with dilute acids can be beneficial to the ICE.[114]

The sodium storage capacity and SEI formation is greatly influenced by the nature of surface oxygen functionalisation of HCs. The coexistence of different OFGs on the surface makes it hard to discriminate between the effects of each individual functionality. To address this issue, Wang *et al.*[115] employed a mechano-chemical post-treatment of anthracite derived HCs by ball milling in CO_2 atmosphere to selectively introduce carboxyl-groups on the surface. During ball milling, CO_2 molecules react with the freshly generated edge sites, thereby increasing the O-content from ~5 at% to 20 at%. They were able to demonstrate an independence between the presence of carboxyl functionalities and the SEI formation. The ball-milled samples exhibited similar ICEs of ~48% whether they were milled in an argon or CO_2 environment. Therefore, they ascribe the charge-loss during the first cycle to the surface area and porosity of the HC.

Surface modification of HCs can also be achieved by wet-chemical impregnation treatments. Li *et al.*[116] immersed HC in an aqueous 2,2-dimethylvinyl boric acid solution to achieve an *in situ* polymerisation during the first cycles, serving as an artificial SEI. The B–OH functionalities react with the inherent protic oxygen surface functionalities, such as –OH and –COOH, and polymerise in the first cycles to a stable polymer network. Therefore, a thinner SEI is formed, and the ICE increased from 65.2 to 77.2% (Figure 6f). A different *in situ* polymerisation approach was pursued by Liu *et al.*[117] by grafting caffeic acid on the surface of HC. Caffeic acid molecules are chemically bound to the surface by a dehydration condensation reaction with already existing OFGs. During the first discharge cycle, caffeic acid molecules form a polymeric film through anionic polymerisation leading to a C=O rich SEI. They report that surface treatment of HC with 15 wt% caffeic acid could increase the ICE from 69% to 93.2%. Romero-Cano *et al.*[118] functionalised HC surface from grapefruit peels with amino groups by a two-step wetness impregnation method with subsequent annealing. A solution containing citric acid was used to introduce carboxyl groups to the HC surface, which undergo an amination reaction with urea or melamine in the second step.

After annealing, the nitrogen functionalisation of the HC improves the ICE from 25 to 60%.

Table 3 summarises different surface modification methods and compares the ICEs. To draw a conclusion, there are many different approaches to manipulate the surface of HCs with varying effects. Comparison across literature is however rather complicated, as numerous different precursors, pyrolysis temperatures and electrolyte systems are used, which all influence the electrochemical performance. Furthermore, studies focusing on the effect of surface OFGs should verify that the morphology is unaffected by their treatment. Otherwise, the assumed effects of the treatment cannot be attributed to the surface modification.

3.5. Advanced Characterisation techniques for HC electrodes

An important factor in understanding how defects work is not only controlled fabrication, but also the application of advanced characterisation techniques. While techniques such as NMR or *operando* Raman spectroscopy have been used to analyse HC electrodes, there are few studies reporting such mechanistic experimental investigations for the felt electrodes used in VFBs.[123,124] Therefore, we will shortly discuss some general ideas and topics for understanding defects in HC and encourage the interested reader to consider this as a topic for future review articles.

Carbon-based electrodes exhibit complex electrochemical behaviour that is influenced by the presence of defects. To gain a mechanistic understanding of these electrodes, operando techniques have proven to be powerful tools to study their electronic and (electro)chemical properties in real time and under realistic operating conditions.[125] Understanding the intercalation mechanism of sodium ions in HC is crucial for the further development of SIBs.[126] Sodium intercalation in graphite is thermodynamically hindered, so that graphite cannot be used as a negative electrode material in SIBs; on the other hand, the intercalation of sodium is energetically favoured over lithium and potassium.[127] Mechanistic insights enable precise development of the material in question and optimisation of its performance by adjusting its structure and properties to improve ion storage capacity, cycling stability and overall battery efficiency. Therefore, the study of the sodiation mechanism is not only a topic well suited for operando methods, but also of great importance for research. An overview of operando spectroscopy on carbon-free SIB anodes can be found elsewhere.[128]

Raman spectroscopy proves particularly well-suited for this purpose due to its utilisation of visible light, which makes experiments possible under ambient conditions Hence, it has

Table 3. Surface treatments and electrochemical performances.

HC precursor	Pyrolysis Temperature	Surface Treatment	Electrolyte	ICE [%]	Ref
Anthracite	1600 °C	(i) CO_2 atm. ball milling	1 M $NaClO_4$ EC:PC:FEC	47.7	[115]
		(ii) Ar atm. ball milling		47.9	
		(iii) H_2SO_4 and HNO_3 (3:1, v/v) at 70 °C		71.4	
Cellulose	1000 °C	(i) CO_2 atm. ball milling	1 M $NaClO_4$ EC:DEC	39.5	[119]
		(ii) 1. CO_2 atm. ball milling, 2. reduction in H_2/Ar atm.		21.5	
Sucrose/phenol formaldehyde resin	1300 °C	(i) Pyrolysis in cyclohexane vapours/Ar	0.8 M $NaPF_6$ EC:DMC	85	[112]
		(ii) Pyrolysis in ethanol vapours/Ar		79	
		(iii) 1. Pyrolysis in cyclohexane vapours/Ar, 2. HCl / HNO_3		30	
Cellulose	1400 °C	–	1 M $NaPF_6$ EC:DMC	82.7	[107]
		Conc. HNO_3 at 60 °C		55.9	
		(iii) 1. Conc. HNO_3 at 60 °C, 2. 900 °C under H_2		48.2	
Sucrose	1200 °C	in-situ polymerisation with 3% DEBA	1 M $NaPF_6$ EC:DEC	77.2	[116]
Grapefruit-peels	600 °C	Citric acid, urea	1 M $NaPF_6$ EC:PC:DMC	60	[118]
Glucose	1400 °C	Carbon vapour coating with polypropylene	1 M $NaClO_4$ EC:DEC	81	[120]
Sucrose	1300 °C	O_2 plasma	1 M $NaClO_4$ EC:PC	65.9	[121]
Glucose	900 °C	H_2SO_4 / $KMnO_4$	1 M $NaClO_4$ EC:PC:FEC	41.7	[122]
Potassium citrate	750 °C	dilute HNO_3	1 M $NaClO_4$ EC:PC	81.5	[114]
Xylose	1200 °C	grafting of polymerised caffeic acid	1 M $NaPF_6$ EC:DEC	93.2	[117]

garnered significant favour for numerous electrochemical systems, such as batteries and electrocatalysis. It is applied for diverse phenomena, such as the oxygen evolution reaction in metal oxides,[129] the lithiation[130] and sodiation[131] in carbon-based electrodes, carbon dioxide reduction on copper,[132] and the vanadyl oxidation on carbon paper[123] and graphite.[124]

Reddy et al.[131] and Euchner et al.[133] used operando Raman spectroscopy to investigate the intercalation mechanism and the storage process in HC. Similar to graphite, HC also exhibits a G-band associated with a first-order longitudinal optical phonon mode (E_{2g}), which resembles the in-plane stretching of C=C bonds, and a D-band caused by disorder such as edges, stacking faults or atomic defects, which corresponds to an A_{1g} breathing mode of a C ring.[134] They found that at lower voltages, the D-band disappears and maintains a constant position, while the G-band shifts to lower wavenumbers. In conjunction with DFT calculations, they concluded that sodium intercalation proceeds in four steps: (i) adsorption on reactive surfaces and defect sites, (ii) intercalation in layers - first in defect sites, (iii) filling of the layers, (iv) pooling of nanopores.

Weaving et al.[135] used operando microbeam Raman spectroscopy to gain deeper insights into the mechanisms of sodium incorporation in HC. They found that sodium uptake, especially in the initial stages of the stress profile, occurs by intercalation into the turbostratic nanodomains of carbon. The gradual and reversible changes in the G- and D-Raman peaks suggest that the capacitance comes from complete intercalation, meaning that the entire domain is occupied and not just the surfaces. Since sodium clusters form in the low-voltage plateau, rational pore design, such as the transition from micropores to mesopores, could improve diffusion. They also pointed out the reversibility of the D-peak during (de)intercalation.

Huang et al.[136] used N-doped HC to compare the intercalation kinetics of sodium and lithium with operando Raman spectroscopy. They found that the intercalation of gas ions affects the shape, intensity and position of both the D and G bands. A lower intensity of the D signal was associated with the occupation of defective sites by Li^+/Na^+ ions. The red shift of the G peak was associated with the charge transfer effect through the adsorbed ions. When lithium is used as a guest, the shrinkage of the G band at high voltages is due to weakened resonances as the carbon surface is almost completely covered by intercalated ions. However, no such shrinkage is observed when sodium is used. Therefore, it was concluded that the storage mechanism for sodium ions in hard carbon is based only on adsorption and not on intercalation.

An extensive list of references specifically addressing the capabilities of in situ Raman spectroscopy can be found elsewhere: Cheng et al.[137] highlight the significant contribution of in situ Raman spectroscopy to a better understanding of carbon materials as anodes for alkali metal ion batteries. In particular, the technique allows direct observation of vibrational mode shifts in the carbon material when alkali metal ions are intercalated and de-intercalated during charge and discharge cycles.

Bray et al.[138] performed operando ^{23}Na NMR spectroscopy as well as ^{1}H and ^{23}Na MRI during cycling. ^{23}Na NMR spectroscopy during cycling of half a cell showed that new sodium environments formed during the charging process. The $^{23}Na/^{1}H$-MRI showed the formation and distribution of dendrites at high discharge rates. With full cells, they were able to follow both the formation and the two phases of sodium intercalation in HC at 0 to 2.5 V and 2.5 to 3.7 V, respectively. In the early stages of intercalation, they found signals corresponding to metallic sodium, which later shifts and disappears. Gotoh et al.[139] investigated the overcharging of lithium- and sodium-based batteries using $^{7}Li/^{23}Na$ NMR spectroscopy. In contrast to graphite, where over-lithiation and dendrite growth occur rapidly, quasi-metallic lithium and sodium in HC serve as a buffer for deposition and form reversible dendrites.

A detailed review of such advanced characterisation techniques concerning many more kinetic mechanisms in SIBs and VFBs should be considered soon.

4. Edge site defects and heteroatom doping of graphite for vanadium flow batteries

Vanadium flow batteries (VFBs) for energy storage have the advantage of good safety, decoupled power and energy densities, and long cycling lifetime (>20 years) compared to other battery technologies, such as Li-ion.[140] These batteries consist of V^{2+}/V^{3+} and VO^{2+}/VO_2^+ redox electrolyte solutions which are pumped through electrodes and separated by a membrane (most often a cation-exchange membrane).[141] Each cell in the battery stack contains a positive and negative electrode, where each redox reaction facilitates the transfer of electrons for energy storage and discharge.[142] The electrode performance dictates the power density and battery energy efficiency and can be optimised by fine-tuning electrode design and further surface treatment.[143]

Porous carbon-based materials are commonly used for the VFB electrodes due to their chemical stability, good conductivity, and high surface area.[6,143,144] However, the reaction kinetics of these materials are often poor and therefore require further treatment to enhance the electrode surface to better facilitate the vanadium reactions. Common treatment methods include thermal,,[145–147] chemical,[46,148–151] electrochemical oxidation,[32,152] etching,[153] the deposition of metals[154] and metal oxides,[56,155] and the use of nanomaterials such as CNTs.[57,59,156] These methods aim to modify the chemical composition, surface structure, electrochemically active surface area, conductivity, wettability, or a combination of these characteristics. Defective carbon electrode materials for the VFB have become of great interest as the catalytic nature of defects and edge sites have been found to be active for the vanadium redox reactions.[19–21,32,33,57,157] The introduction of defects and edge sites can often result in changes to the chemical and physical structure of the electrode surface and can be introduced by various treatment methods.

4.1. Defect engineering of carbon electrodes for the VFB

Early research into the enhancement of VFB electrodes almost solely focused on exploring methods which altered the oxygen content at the electrode surface. Initial studies by Sun et al. on thermal and chemical treatment methods attributed an increase in OFGs to enhanced performance.[147,148,150] However, more recent studies have since found that the introduction of carbon defects can also occur during various electrode treatments and may equally be responsible for promoting charge transfer.[19–21,32,33,50,57,59,151,157–159] As a result, the catalytic nature of defective carbon, usually consisting of lattice vacancies and exposed edge sites, has been more thoroughly explored in literature. Pour *et al.* investigated the influence of edge and basal carbon for both graphene and CP (pristine and thermally-treated) and found that an increase in surface defects and oxygenated edge sites helped to better facilitated the vanadium redox reactions (Figure 7a).[154] This is similar to a study done by Langner *et al.*, where the influence of graphitisation temperature (1500–2000 °C, inert environment) and subsequent thermal treatment (400–600 °C, air environment) on the graphitic carbon structure of CF was investigated.[158] It was reported that an increase in electrode kinetics was attributed to an increase in graphitic edge sites and OFGs formed at carbon edges following the thermal treatment step. Mazúr *et al.* evaluated the ohmic and charge-transfer resistances of positive and negative vanadium reactions for thermally-treated felt electrodes.[146] Both defect density and OFGs were maximised for the GF (treated at 500 °C) that exhibited the best electrochemical performance and lowest overall resistance. When the resistances of each vanadium reaction were deconvoluted a decrease in charge-transfer resistance for the negative electrode following an increase in defect density and OFGs from thermal treatment was especially prominent (Figure 7b).

Modifying electrode materials with chemical and etching methods can induce changes in the carbon surface and chemical composition. He *et al.* found that both the oxygen content and defect density increased after a GF was treated with a HF/H_2O_2 solution, with the higher defect density thought to be induced by the introduced OFGs.[151] The energy efficiency and discharge capacity were both improved when the treated GF was used as the positive electrode in a full-cell configuration, and the authors concluded that the increase in defective carbon was beneficial for reducing the electrochemical polarisation of the positive vanadium reaction. A similar relationship between OFGs and carbon defects was found by Park *et al.*,[19] where GF was etched *via* a NiO/Ni redox reaction cycle to produce highly porous, graphenated felt electrodes. SEM, TEM, and Raman spectroscopy were used to show an increase in defective edge sites at the carbon surface following the NiO/Ni treatment (Figure 7c). It was concluded that the presence of carbon defect sites and edge planes facilitated the formation of OFGs (specifically hydroxyl groups) to produce a high density of oxygen-functionalised defects.

The use of nanomaterials to modify VFB electrodes has also become popular, with their purpose usually to increase the available surface area, improve conductivity, and provide additional active sites.[160] A study by Park *et al.*[50] found significant improvement when a nanofibre/nanotube composite was deposited onto CF, with the improved electrode performance attributed to the increase in surface defect density of the nanofibres and fast electron-transfer rate of the nanotube wall basal plane (Figure 7d). Fu *et al.*[57] investigated graphene-modified CF, with an improvement in reaction kinetics and electronic conductivity attributed to the increased number of exposed graphene edges and OFGs. The oxygen-functionalised carbon defects were thought to induce electron redistribution due the electronegativity difference between C and O atoms, investigated via spin-polarised DFT calculations (Figure 7e). Another study looked at GF decorated with carbon dots and concluded that abundant defect sites at the carbon dot surface and the improved hydrophilicity was responsible for enhanced electrode performance.[59] It is clear from these studies that introducing defective carbon improves electrode performance, however, there is little selectivity and other features such as oxygen functionality make it hard to determine the true catalytic centre.

While many studies suggest that OFGs are beneficial, others have reported that they either have little to no effect[21,146] or hinder[20,32,159,161] one or both vanadium redox reactions, with carbon defects and edge sites found to be the relevant catalytic sites. Of these studies, it is typically the positive vanadium reaction which is found to be catalysed by carbon defects rather than OFGs. However, the formation of OFGs and carbon defects are often reported to occur simultaneously,[19,32,158] therefore, their respective roles in facilitating the vanadium reactions can be difficult to deconvolute. In one study, Fink *et al.* investigated the influence of oxygen groups by comparing the performance of pristine and thermally-treated GFs, with electrochemical impedance spectroscopy (EIS) used to evaluate the charge-transfer resistance of each electrode.[159] The normalised rate constant of each vanadium redox reaction was found to increase for either an increase in OFGs (V^{2+}/V^{3+}) or graphitic carbon (VO^{2+}/VO_2^{+}) (Figure 8a). However, the measured graphitic carbon content (found *via* XPS) did not differentiate between carbon type or bonding and therefore the carbon defect density was not directly measured. Maruyama et al. used a fine-etching technique to introduce edge sites to a graphitised carbon fibre surface, with these exposed edge sites thought to be responsible for improving the activity of both vanadium reactions.[157] A study by Cao *et al.* on the influence of initial surface pre-treatment of glassy carbon found that surface roughness and defects produced *via* mechanical polishing increased the electrochemical activity for the positive vanadium reaction.[32] It was also reported that during electrochemical oxidation treatment both electrode surface roughness and OFGs are introduced. However, it appeared that the electrode activity improved when surface roughness was more prominent and decreased when OFGs were more prominent.

The catalytic nature of defective carbon has also been investigated via oxygenation and deoxygenation processes to try and deconvolute defects and OFGs. Radinger *et al.* thermally treated both pristine and surface-activated (high OFG and defect content) GF under reductive (Ar/H_2) conditions.[20] The

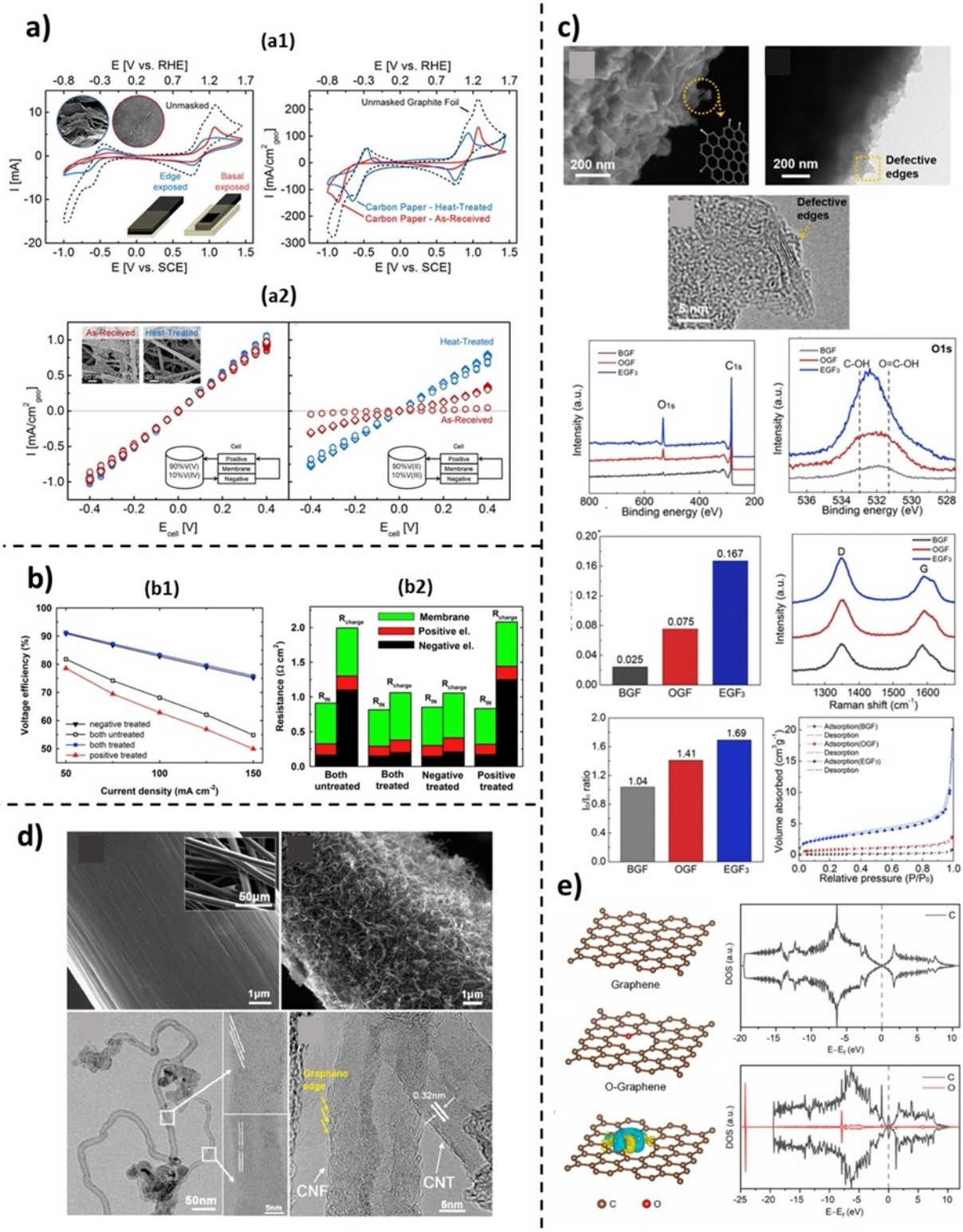

Figure 7. (a) Cyclic voltammetry of pristine and heat-treated graphite foil to determine influence of basal plane versus edge sites (a1) and potentiostatic measurements of CP to determine the effect of beginning-of-life (circles) versus post-measurement (diamonds) (a2). Reprinted with permission from ref. [33] Copyright (2015) ACS. (b) Dependency of voltage efficiency of current density (b1) and distribution of ohmic and charge-transfer resistances (b2). Reprinted with permission from ref. [146] Copyright (2018) Elsevier. (c) SEM, TEM, XPS, Raman, and absorption/desorption characterisation of treated felt electrodes to demonstrate graphite surface containing defective edges. Reprinted with permission from ref. [19] Copyright (2016) Elsevier. (d) SEM and HR-TEM imaging of CNF/CNT-modified electrode surface. Reprinted with permission from ref. [50] Copyright (2013) ACS. (e) Atomic configuration and density of state calculations for defect rich, O-doped graphene. Reprinted with permission from ref. [57] Copyright (2023) Elsevier.

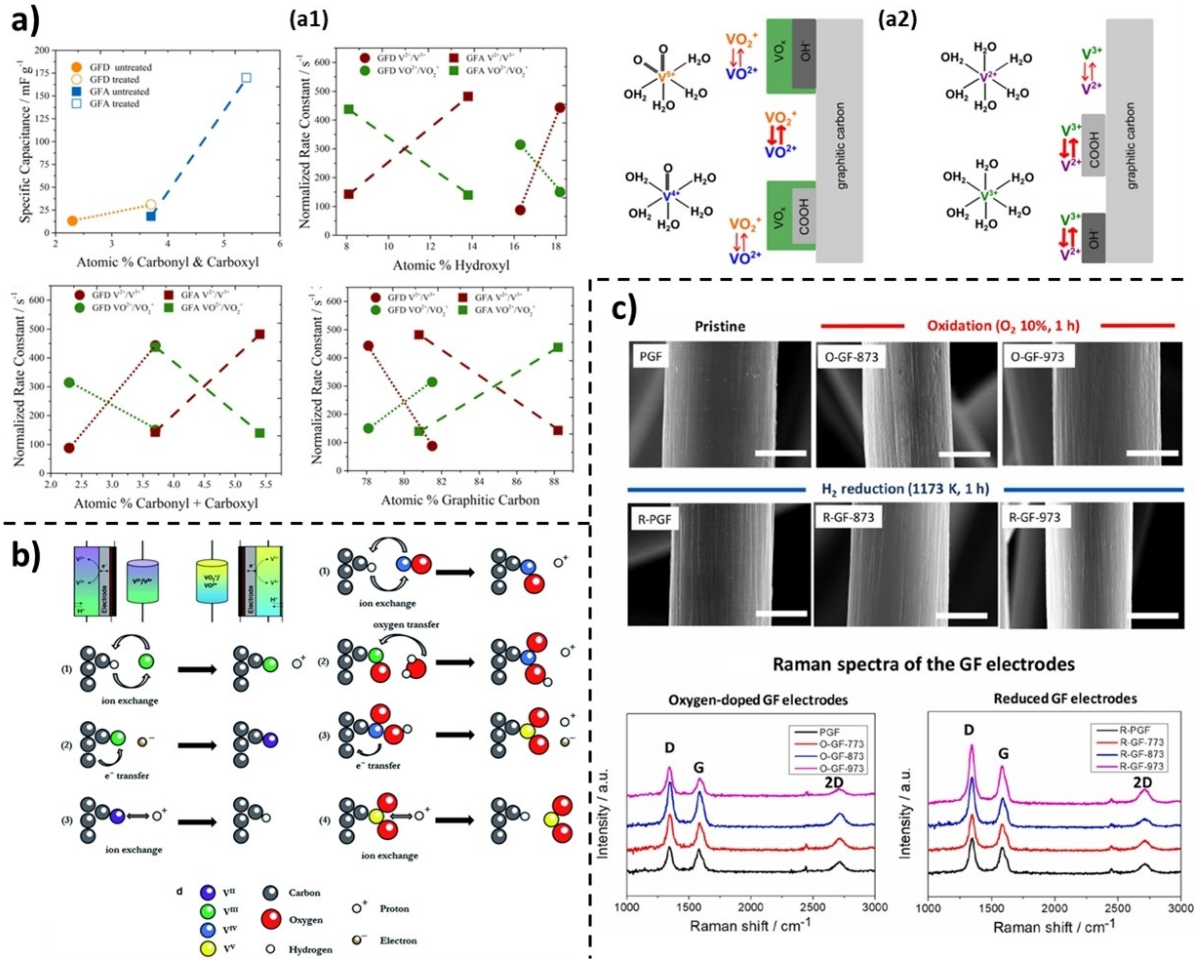

Figure 8. (a) Catalytic role of carbonyl, carboxyl, hydroxyl, and graphitic carbon groups for the positive and negative vanadium redox reactions, as shown by the specific capacitance and normalised rate constant (a1), and proposed reaction mechanisms (a2). Reprinted with permission from Ref. [159] Copyright (2016) ACS. (b) Proposed reaction mechanisms for the positive and negative vanadium redox reactions. Reprinted with permission from Ref. [20] used under Creative Commons CC-BY license. (c) SEM imaging and Raman spectroscopy of pristine, oxygen-doped, and reduced GF electrodes. Reprinted with permission from Ref. [21] Copyright (2022) Elsevier.

presence of carbon defects was found to correlate with improved electrochemical properties, while no positive relationship could be established for any specific OFG or oxygen content in general. It was proposed that the vanadium redox reactions occur preferentially at hydrogen-terminated edge sites (Figure 8b). A similar study by Kim *et al.* used temperature programmed oxidation and reduction (TPO-TPR) to produce GF electrodes which were either oxygenated or deoxygenated.[21] From Raman spectroscopy and XPS analysis, it was determined that the oxidised GF electrode had both carbon defects and an increased oxygen content at the fibre surface, while the reduced GF had only carbon defects present (Figure 8c). During cyclic voltammetry, EIS, and full-cell cycling, both the oxidised and reduced felt electrodes treated at the same temperature exhibited similar performance which suggested that carbon defects were responsible for enhancing the reaction kinetics of both vanadium reactions. Studies which attempt to deconvolute the influence of differing surface functionalisation on reaction kinetics are particularly important as they allow for clear structure-activity correlations to be established.

Although many studies relate the influence of electrode characteristics and half- or full-cell VFB performance to the electronic properties and charge density at the carbon surface, only a few seem to directly probe the electronic state.[22,123,162] One such study used ultraviolet photoelectron spectroscopy (UPS) and reflective electron energy loss spectroscopy (REELS) to determine the electronic properties of GF for the positive vanadium reaction.[22] Carbon edge sites were found to be the main catalytic centre, with changes in the valence band and Fermi level linked to electrode activity. Another study used Raman spectroscopy to determine how different treatments impacted the electronic structure of CP.[162] Changes in the 2D band from the Raman spectra were used to indicate shifts in the Fermi level, with an increase in defect density via nitrogen doping found to favourably decrease the charge-transfer energy barrier. These studies on the interactions between the electronic structure of modified carbon electrodes and the vanadium reactions are beneficial to better understand the role of defective carbon specifically for VFBs.

4.2. Heteroatom doping for defect engineering of VFB electrodes

Modifying electrodes via heteroatom doping is a widely explored area of enhanced electrode activation research, with oxygen[18,163–166] and nitrogen[18,40,43,55,165,167–169] atoms the most common dopants for VFB electrodes. Other less frequently used heteroatoms for doping carbon electrodes include phosphorous,[168,170,171] boron,[18,54,163,168] and sulphur.[39,172] Generally, heteroatom doping aims to increase the number of available active sites, with studies also reporting improved wettability and increased ECSA.[142] Additionally, heteroatom doping can introduce defects to the carbon lattice and so can be a viable pathway for defect engineering. Opar *et al.* modified CF with nitrogen-functionalised mesoporous graphene and found that defects introduced from N-doping improved electrode performance.[55] The modified electrode with the highest I_D/I_G ratio (indicating defect density) was found to exhibit the best activity, even though it did not have the highest nitrogen content (Figure 9a). The enhanced electronic and chemisorption properties were also thought to be partially due to the electronegativity difference between C and N atoms at N-doped sites resulting in a higher charge density. A study investigating P-doped GF carried out by Gursu *et al.*[171] found that better electrode performance was a result of phosphorous-containing groups, as well as defective carbon sites induced by the P-doping procedure. Kim *et al.*[18] reported on N-doped, O-doped, B-doped, and B and N co-doped GFs and attributed the improved electrode performance to defect formation induced by the doping (Figure 9b). Furthermore, the performance of the B and N co-doped GF was significantly better, with the p-n type bonding from the B and N groups thought to contribute a large difference in electronegativity and thus a higher charge density at these sites.

Certain functional groups formed from heteroatom doping are often reported as being more electrochemically active, such

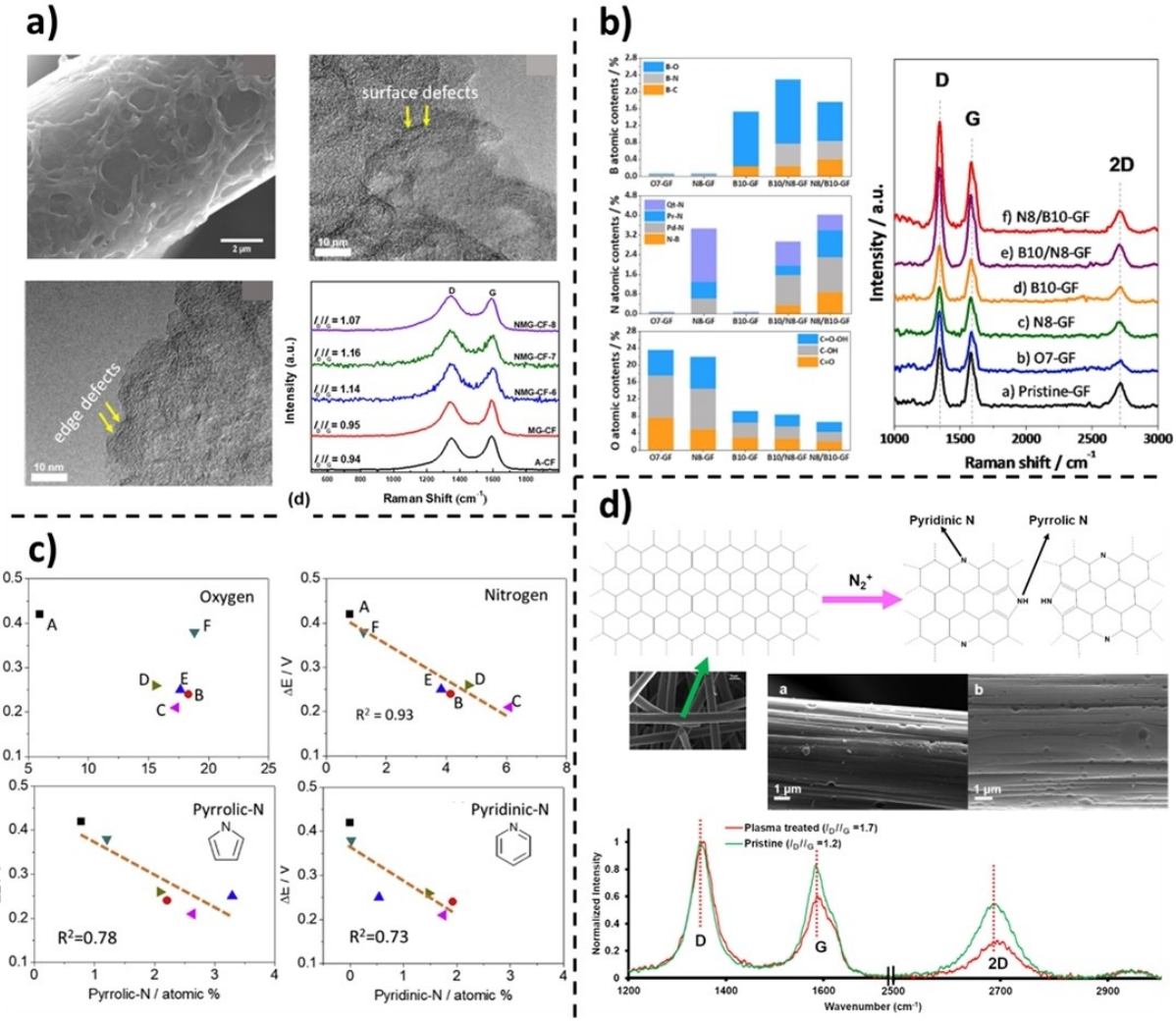

Figure 9. (a) SEM imaging and Raman spectroscopy of N-doped mesoporous GF. Reprinted with permission from Ref. [55] Copyright (2020) Elsevier. (b) Surface atomic content of heteroatom functionalities and Raman spectra of pristine and O-, N-, and/or B-doped GF. Reprinted with permission from Ref. [18] Copyright (2023) Elsevier. (c) Relationship between peak separation (extracted from cyclic voltammetry) and different O- and N-doped GFs. Reprinted with permission from Ref. [165] Copyright (2020) Elsevier. (d) SEM imaging and Raman spectroscopy of N_2-plasma treated GF electrodes. Reprinted with permission from Ref. [43], used under Creative Commons CC-BY license.

as hydroxyls (O-doping), pyridinic-N (N-doping), and pyrrolic-N (N-doping).[19,43,65,165,169,173] Kim *et al.* investigated N and O co-doped GF *via* urea thermolysis and found that pyridinic- and pyrrolic-N groups were the main active centres for the vanadium reactions (Figure 9c).[165] The authors thought that the pyridinic- and pyrrolic-N could induce greater charge delocalisation due to the formation of low coordinated edge-defects and better facilitate chemisorption of the redox species. Another study by the same research group on N and O co-doping attributed enhanced electrode performance to the synergistic effects of N- and O-functionalisation, specifically pyrrolic-N and hydroxyl groups.[166] Dixon et al. used N_2 plasma treatment to introduce defects and nitrogen groups to CF and found an increase in carbon defects, edge sites, and pyrrolic- and pyridinic-N groups all correlated to better electrode kinetics (Figure 9d).[43] Due to the convoluted nature of heteroatom doping and the induced carbon defects it is hard to come to a definite conclusion on whether the heteroatom itself or the defective carbon is the true catalytic centre, which raises a need for more research into the fundamental interactions between carbon defects and vanadium. Nonetheless, it is evident that defective carbon plays a role in catalysing the vanadium reactions, and therefore, future research should focus on incorporating defect sites into VFB electrodes.

5. Summary and Outlook

Research into energy storage technologies has gained considerable attention, with this review focused on the increased efforts put into identifying high-performing defective carbon electrodes for SIBs and VFBs. Techniques for modifying carbon-based electrodes for use in SIBs and VFBs are evaluated, where various methods were found to successfully introduce defects into the carbon lattice. Efforts to improve SIB electrodes in literature mostly concentrate on investigating a wide range of precursors, both naturally and synthetically derived, and heteroatom doping to optimise the performance of HCs. Novel methods for manufacturing defective HCs aim to reduce energy consumption while increasing production rates, although most of these methods still require further development and scale-up. Defect engineering via these methods appeared to increase the interlayer spacing, enhance the porosity and surface chemistry which allows for better sodium intercalation and larger reversible capacities. Furthermore, the introduction of heteroatom functionalisation and methods of surface modification have been reported to improve SEI formation and increase the ICE. For VFBs, electrode enhancement (such as *via* thermal, etching, or catalyst deposition) in literature appears to usually occur post-manufacture, with the introduction of defects thought to improve electrode kinetics, wettability, and electrochemically-active surface area. However, most defect introduction methods also incorporate functional groups, *i.e.*, oxygen, making it difficult to identify the effects of the former compared to the latter. Indeed, recent research has explored the sentiment that oxygen functional groups are the relevant active site, with studies showing how defective carbon sites may be the preferred catalytic centre. Electrospinning methods, which can introduce defects during manufacture, are still lagging and need to be greatly improved in terms of porosity and reproducibility.

From the reviewed research, carbon defects play an important role in facilitating the electrochemical mechanisms that occur within SIBs and VFBs. Thus, future research should focus on incorporating defective carbon sites into electrode materials, as well as probing the intrinsic chemical and electronic properties to better understand the interactions between redox species and carbon defects. Further work into discerning between specific types of carbon defect (*i.e.*, point vacancy, zigzag edge, armchair edge) at the electrode surface may allow for a clearer idea of the role they play in improving SIBs and VFBs. Methods must be established which introduce defects but do not significantly alter the morphology and surface area of the electrode. More controllable methods for introducing defective carbon, both from precursors and post-treatment, could also allow for studies to compare defect density more purposefully, which would greatly benefit endeavours to produce low-cost, high-performance electrodes for battery systems. For SIBs, literature comparison is challenging because there is no consensus about mass loading, electrolyte composition, binders, additives, etc. Additionally, using natural precursors for studies addressing basic structure-property relationships are not meaningful because reproducibility is barely given. Continued research efforts in this area will enable the development of carbon-based electrodes that address the challenges faced by VFBs and SIBs, ultimately paving the way for the widespread adoption of these promising energy storage technologies.

Acknowledgements

Part of this research was funded by NZ Ministry of Business, Innovation and Employment (MBIE) under the contract UOCX2111. This work contributes to the research performed at CELEST (Center for Electrochemical Energy Storage Ulm-Karlsruhe) and was funded by the German Research Foundation (DFG) under Project ID 390874152 (POLiS Cluster of Excellence). Open Access funding enabled and organized by Projekt DEAL.

Conflict of Interests

There is no conflict of interest to report.

Keywords: carbon-based electrodes · sodium-ion batteries · surface chemistry · structure-activity relationships · vanadium flow batteries

[1] a) D. Gielen, F. Boshell, D. Saygin, M. D. Bazilian, N. Wagner, R. Gorini, *Energy Strategy Rev.* **2019**, *24*, 38–50; b) D. Bogdanov, et al., *Energy* **2021**, *227*, 120467.
[2] a) Y. Gao, Z. Pan, J. Sun, Z. Liu, J. Wang, *Nano-Micro Lett.* **2022**, *14*, 94; b) J. Liu, J. Xiao, J. Yang, W. Wang, Y. Shao, P. Liu, M. S. Whittingham,

Next Energy **2023**, *1*, 100015; c) M. Houache, C.-H. Yim, Z. Karkar, Y. Abu-Lebdeh, *Batteries* **2022**, *8*, 70.
[3] D. Kundu, E. Talaie, V. Duffort, L. F. Nazar, *Angew. Chem. Int. Ed.* **2015**, *54*, 3431–3448.
[4] P. Alotto, M. Guarnieri, F. Moro, *Renewable Sustainable Energy Rev.* **2014**, *29*, 325–335.
[5] a) X. Li, X. Sun, X. Hu, F. Fan, S. Cai, C. Zheng, G. D. Stucky, *Nano Energy* **2020**, *77*, 105143; b) T. Perveen, M. Siddiq, N. Shahzad, R. Ihsan, A. Ahmad, M. I. Shahzad, *Renewable Sustainable Energy Rev.* **2020**, *119*, 109549; c) X.-F. Luo, C.-H. Yang, Y.-Y. Peng, N.-W. Pu, M.-D. Ger, C.-T. Hsieh, J.-K. Chang, *J. Mater. Chem. A* **2015**, *3*, 10320–10326; d) A. W. Bayeh, D. M. Kabtamu, Y.-C. Chang, T. H. Wondimu, H.-C. Huang, C.-H. Wang, *Sustain. Energy Fuels* **2021**, *5*, 1668–1707.
[6] M. Gencten, Y. Sahin, *Int. J. Energy Res.* **2020**, *44*, 7903–7923.
[7] a) R. L. McCreery, *Chem. Rev.* **2008**, *108*, 2646–2687; b) F. Rodríguez-reinoso, *Carbon* **1998**, *36*, 159–175.
[8] a) G. Kothandam, et al., *Adv. Sci.* **2023**, *10*, e2301045; b) H. Yin, H. Shao, B. Daffos, P.-L. Taberna, P. Simon, *Electrochem. Commun.* **2022**, *137*, 107258; c) R. C. Massé, C. Liu, Y. Li, L. Mai, G. Cao, *Natl. Sci. Rev.* **2017**, *4*, 26–53; d) S. Qiu, et al., *Adv. Energy Mater.* **2017**, *7*, 1700403.
[9] S. Mukherjee, S. Bin Mujib, D. Soares, G. Singh, *Materials (Basel)* **2019**, *12*.
[10] Q. Liu, Z. Hu, C. Zou, H. Jin, S. Wang, L. Li, *Cell Rep. Phys. Sci.* **2021**, *2*, 100551.
[11] Y. Wu, R. Holze, *Batteries* **2018**, *4*, 47.
[12] J. Xu, Y. Zhang, Z. Huang, C. Jia, S. Wang, *Energy Fuels* **2021**, *35*, 8617–8633.
[13] E. Olsson, J. Cottom, Q. Cai, *Small* **2021**, *17*, e2007652.
[14] Y. Chen, F. Li, Z. Guo, Z. Song, Y. Lin, W. Lin, L. Zheng, Z. Huang, Z. Hong, M.-M. Titirici, *J. Power Sources* **2023**, *557*, 232534.
[15] Q. Wang, X. Ge, J. Xu, Y. Du, X. Zhao, L. Si, X. Zhou, *ACS Appl. Energ. Mater.* **2018**, *1*, 6638–6645.
[16] Z. Li, Y. Chen, Z. Jian, H. Jiang, J. J. Razink, W. F. Stickle, J. C. Neuefeind, X. Ji, *Chem. Mater.* **2018**, *30*, 4536–4542.
[17] T. W. Surta, E. Koh, Z. Li, D. B. Fast, X. Ji, P. A. Greaney, M. R. Dolgos, *Adv. Energy Mater.* **2022**, *12*, 2200647.
[18] H. Kim, J. Paick, J. S. Yi, D. Lee, *J. Power Sources* **2023**, *557*, 232612.
[19] J. J. Park, J. H. Park, O. O. Park, J. H. Yang, *Carbon* **2016**, *110*, 17–26.
[20] H. Radinger, A. Ghamlouche, H. Ehrenberg, F. Scheiba, *J. Mater. Chem. A* **2021**, *9*, 18280–18293.
[21] S.-C. Kim, J. Paick, J. S. Yi, D. Lee, *J. Power Sources* **2022**, *520*, 230813.
[22] H. Radinger, V. Trouillet, F. Bauer, F. Scheiba, *ACS Catal.* **2022**, *12*, 6007–6015.
[23] Z. Zhao, H. Chen, W. Zhang, S. Yi, H. Chen, Z. Su, B. Niu, Y. Zhang, D. Long, *Mater Adv* **2023**, *4*, 835–867.
[24] Y. Zhang, J. Xu, Y. Long, L. Tao, M. Ding, C. Jia, *ChemNanoMat* **2020**, *6*, 1589–1600.
[25] a) H. Li, R. Li, J. Niu, K. Gan, X. He, *Front. Chem.* **2022**, *10*, 1067327; b) X. Yan, Y. Jia, X. Yao, *Chem. Soc. Rev.* **2018**, *47*, 7628–7658; c) Y. Xu, X. Liu, N. Cao, X. Xu, L. Bi, *Sustain. Mater. Technol.* **2021**, *27*, e00229.
[26] L. Zhang, Y. Jia, X. Yan, X. Yao, *Small* **2018**, *14*, e1800235.
[27] J. Zhu, S. Mu, *Adv. Funct. Mater.* **2020**, *30*, 2001097.
[28] a) C. Xie, D. Yan, W. Chen, Y. Zou, R. Chen, S. Zang, Y. Wang, X. Yao, S. Wang, *Mater. Today* **2019**, *31*, 47–68; b) G. Kudur Jayaprakash, N. Casillas, P. D. Astudillo-Sánchez, R. Flores-Moreno, *J. Phys. Chem. A* **2016**, *120*, 9101–9108.
[29] Y. Jia, J. Chen, X. Yao, *Mater. Chem. Front.* **2018**, *2*, 1250–1268.
[30] J. Zhang, J. Zhang, F. He, Y. Chen, J. Zhu, D. Wang, S. Mu, H. Y. Yang, *Nano-Micro Lett.* **2021**, *13*, 65.
[31] a) S. Zhao, Z. Guo, J. Yang, C. Wang, B. Sun, G. Wang, *Small* **2021**, *17*, e2007431; b) Y. Zhang, L. Tao, C. Xie, D. Wang, Y. Zou, R. Chen, Y. Wang, C. Jia, S. Wang, *Adv. Mater.* **2020**, *32*, e1905923.
[32] L. Cao, M. Skyllas-Kazacos, D.-W. Wang, *J. Electrochem. Soc.* **2016**, *163*, A1164–A1174.
[33] N. Pour, D. G. Kwabi, T. Carney, R. M. Darling, M. L. Perry, Y. Shao-Horn, *J. Phys. Chem. C* **2015**, *119*, 5311–5318.
[34] a) S. Tan, et al., *Molecules* **2023**, *28*, 3134; b) Q. Wu, X. Yan, Y. Jia, X. Yao, *EnergyChem* **2021**, *3*, 100059.
[35] V. A. Kislenko, S. V. Pavlov, S. A. Kislenko, *Electrochim. Acta* **2020**, *341*, 136011.
[36] J. P. V. Tafoya, M. Thielke, G. Tian, R. Jervis, A. B. J. Sobrido, *Curr. Opin. Chem. Eng.* **2022**, *38*, 100876.
[37] a) X. L. Zhou, Y. K. Zeng, X. B. Zhu, L. Wei, T. S. Zhao, *J. Power Sources* **2016**, *325*, 329–336; b) S. Abbas, S. Mehboob, H.-J. Shin, O. H. Han, H. Y. Ha, *Chem. Eng. J.* **2019**, *378*, 122190.
[38] H. R. Jiang, J. Sun, L. Wei, M. C. Wu, W. Shyy, T. S. Zhao, *Energy Storage Mater.* **2020**, *24*, 529–540.
[39] Z. Xu, M. Zhu, K. Zhang, X. Zhang, L. Xu, J. Liu, T. Liu, C. Yan, *Energy Storage Mater.* **2021**, *39*, 166–175.
[40] S. J. Yoon, S. Kim, D. K. Kim, D. M. Yu, R. Hempelmann, Y. T. Hong, S. So, *Energy Fuels* **2020**, *34*, 5052–5059.
[41] T. H. Noh, M. Y. Kim, D. H. Kim, S. H. Yang, J. H. Lee, H. S. Park, H. S. Noh, M. S. Lee, H. S. Kim, *J. Electrochem. Sci. Technol* **2017**, *8*, 155–161.
[42] J. Xu, et al., *J. Cent. South Univ.* **2022**, *29*, 2956–2967.
[43] D. Dixon, D. J. Babu, A. Bhaskar, H.-M. Bruns, J. J. Schneider, F. Scheiba, H. Ehrenberg, *Beilstein J. Nanotechnol.* **2019**, *10*, 1698–1706.
[44] a) T. Jirabovornwisut, B. Singh, A. Chutimasakul, J.-H. Chang, J.-Z. Chen, A. Arpornwichanop, Y.-S. Chen, *Materials (Basel)* **2021**, *14*; b) D. Dixon, D. J. Babu, J. Langner, M. Bruns, L. Pfaffmann, A. Bhaskar, J. J. Schneider, F. Scheiba, H. Ehrenberg, *J. Power Sources* **2016**, *332*, 240–248.
[45] C.-H. Lin, Y.-D. Zhuang, D.-G. Tsai, H.-J. Wei, T.-Y. Liu, *Polymer* **2020**, *12*, 1372.
[46] X. Wu, Z. Xie, H. Zhou, Z. Xiong, X. Yin, H. Tang, Q. Ma, J. Liao, *Electrochim. Acta* **2023**, *440*, 141728.
[47] a) X. Luo, H. Zheng, W. Lai, P. Yuan, S. Li, de Li, Y. Chen, *Energy Environ. Mater.* **2023**, *6*; b) F. Banhart, J. Kotakoski, A. V. Krasheninnikov, *ACS Nano* **2011**, *5*, 26–41.
[48] a) S. Dissegna, K. Epp, W. R. Heinz, G. Kieslich, R. A. Fischer, *Adv. Mater.* **2018**, *30*, e1704501; b) O. V. Yazyev, S. G. Louie, *Phys. Rev. B* **2010**, *81*.
[49] a) Z. Tan, et al., *Adv. Mater.* **2017**, *29*; b) D. Cheng, Z. Wang, C. Chen, K. Zhou, *Carbon* **2019**, *145*, 38–46.
[50] M. Park, Y. Jung, J. Kim, H. i. Lee, J. Cho, *Nano Lett.* **2013**, *13*, 4833–4839.
[51] Q. Deng, et al., *Adv. Energy Mater.* **2022**, *12*, 2103186.
[52] R. R. Jacquemond, C. T.-C. Wan, Y.-M. Chiang, Z. Borneman, F. R. Brushett, K. Nijmeijer, A. Forner-Cuenca, *Cell Rep. Phys. Sci.* **2022**, *3*, 100943.
[53] E.-M. Hammer, B. Berger, L. Komsiyska, *IJRED* **2014**, *3*, 7–12.
[54] S. E. Park, S. Y. Yang, K. J. Kim, *Appl. Surf. Sci.* **2021**, *546*, 148941.
[55] D. O. Opar, R. Nankya, J. Lee, H. Jung, *Appl. Surf. Sci.* **2020**, *531*, 147391.
[56] D. M. Kabtamu, Y.-Z. Li, A. W. Bayeh, Y.-T. Ou, Z.-J. Huang, T.-C. Chiang, H.-C. Huang, C.-H. Wang, *ACS Appl. Energ. Mater.* **2023**, *6*, 3301–3311.
[57] H. Fu, X. Bao, M. He, J. Xu, Z. Miao, M. Ding, J. Liu, C. Jia, *J. Power Sources* **2023**, *556*, 232443.
[58] T. Long, Y. Long, M. Ding, Z. Xu, J. Xu, Y. Zhang, M. Bai, Q. Sun, G. Chen, C. Jia, *Nano Res.* **2021**, *14*, 3538–3544.
[59] Y. Zhou, Le Liu, Y. Shen, L. Wu, L. Yu, F. Liang, J. Xi, *Chem. Commun.* **2017**, *53*, 7565–7568.
[60] B. Huang, Y. Liu, M. Xia, J. Qiu, Z. Xie, *Sustain. Energy Fuels* **2020**, *4*, 559–570.
[61] L. Wu, Y. Shen, L. Yu, J. Xi, X. Qiu, *Nano Energy* **2016**, *28*, 19–28.
[62] Z. Tai, D. Ju, S. Sato, K. Hanawa, *Coating* **2021**, *11*, 736.
[63] K. Mushtaq, S. Delgado, A. Mendes, *J. Energy Storage* **2023**, *65*, 107234.
[64] A. Alazmi, C. T.-C. Wan, P. M. Costa, F. R. Brushett, *J. Energy Storage* **2022**, *50*, 104192.
[65] Y. Li, S. Yang, Y. Zhao, N. Mubarak, M. Xu, M. Ihsan-Ul-Haq, T. Zhao, Q. Chen, J.-K. Kim, *J. Mater. Chem. A* **2022**, *10*, 5605–5613.
[66] M. Maleki, G. A. El-Nagar, D. Bernsmeier, J. Schneider, C. Roth, *Sci. Rep.* **2020**, *10*, 11153.
[67] I. Mustafa, R. Susantyoko, C.-H. Wu, F. Ahmed, R. Hashaikeh, F. Almarzooqi, S. Almheiri, *Sci. Rep.* **2019**, *9*, 17655.
[68] M. Maleki, T. Tichter, G. A. El-Nagar, I. Lauermann, C. Roth, *ChemElectroChem* **2021**, *8*, 218–226.
[69] J. Sun, L. Zeng, H. R. Jiang, C. Chao, T. S. Zhao, *J. Power Sources* **2018**, *405*, 106–113.
[70] Y. Zhang, X. Zhang, Z. Xu, D. Zhang, W. Yu, Y. Zhang, L. Liu, J. Liu, C. Yan, *J. Power Sources* **2022**, *552*, 232241.
[71] C. T.-C. Wan, R. R. Jacquemond, Y.-M. Chiang, K. Nijmeijer, F. R. Brushett, A. Forner-Cuenca, *Adv. Mater.* **2021**, *33*, e2006716.
[72] N. Wang, Y. Wang, X. Xu, T. Liao, Y. Du, Z. Bai, S. Dou, *ACS Appl. Mater. Interfaces* **2018**, *10*, 9353–9361.
[73] Q. Meng, Y. Lu, F. Ding, Q. Zhang, L. Chen, Y.-S. Hu, *ACS Energy Lett.* **2019**, *4*, 2608–2612.
[74] Nagmani, A. Tyagi, S. Puravankara, *Mater Adv* **2022**, *3*, 810–836.
[75] K. Wang, Y. Jin, S. Sun, Y. Huang, J. Peng, J. Luo, Q. Zhang, Y. Qiu, C. Fang, J. Han, *ACS Omega* **2017**, *2*, 1687–1695.
[76] Y. Zhen, Y. Chen, F. Li, Z. Guo, Z. Hong, M.-M. Titirici, *Proc. Natl. Acad. Sci. USA* **2021**, *118*.

[77] F. Zhang, Y. Yao, J. Wan, D. Henderson, X. Zhang, L. Hu, *ACS Appl. Mater. Interfaces* **2017**, *9*, 391–397.
[78] a) B. Zhang, M. Deschamps, M.-R. Ammar, E. Raymundo-Piñero, L. Hennet, D. Batuk, J.-M. Tarascon, *Adv. Mater. Technol.* **2017**, *2*, 1600227; b) L. Zhao, Z. Liu, D. Chen, F. Liu, Z. Yang, X. Li, H. Yu, H. Liu, W. Zhou, *Nano-Micro Lett.* **2021**, *13*, 49.
[79] R. M. N. M. Rathnayake, T. T. Duignan, D. J. Searles, X. S. Zhao, *Phys. Chem. Chem. Phys.* **2021**, *23*, 3063–3070.
[80] P. GE, *Solid State Ionics* **1988**, *28–30*, 1172–1175.
[81] D. A. Stevens, J. R. Dahn, *J. Electrochem. Soc.* **2000**, *147*, 1271.
[82] C. Bommier, T. W. Surta, M. Dolgos, X. Ji, *Nano Lett.* **2015**, *15*, 5888–5892.
[83] J. Li, T. Li, C. Peng, J. Li, H. Zhang, *J. Electrochem. Soc.* **2022**, *169*, 70517.
[84] K. Wang, Y. Xu, Y. Li, V. Dravid, J. Wu, Y. Huang, *J. Mater. Chem. A* **2019**, *7*, 3327–3335.
[85] M. Song, Q. Song, T. Zhang, X. Huo, Z. Lin, Z. Hu, L. Dong, T. Jin, C. Shen, K. Xie, *Nano Res.* **2023**, *16*, 9299–9309.
[86] A. Beda, F. Rabuel, M. Morcrette, S. Knopf, P.-L. Taberna, P. Simon, C. Matei Ghimbeu, *J. Mater. Chem. A* **2021**, *9*, 1743–1758.
[87] L. Xiao, H. Lu, Y. Fang, M. L. Sushko, Y. Cao, X. Ai, H. Yang, J. Liu, *Adv. Energy Mater.* **2018**, *8*, 1703238.
[88] H. Au, et al., *Energy Environ. Sci.* **2020**, *13*, 3469–3479.
[89] R. Morita, K. Gotoh, K. Kubota, S. Komaba, K. Hashi, T. Shimizu, H. Ishida, *Carbon* **2019**, *145*, 712–715.
[90] Y. Katsuyama, Y. Nakayasu, H. Kobayashi, Y. Goto, I. Honma, M. Watanabe, *ChemSusChem* **2020**, *13*, 5762–5768.
[91] C. Nita, B. Zhang, J. Dentzer, C. Matei Ghimbeu, *J. Energy Chem.* **2021**, *58*, 207–218.
[92] A. Kamiyama, K. Kubota, T. Nakano, S. Fujimura, S. Shiraishi, H. Tsukada, S. Komaba, *ACS Appl. Energ. Mater.* **2020**, *3*, 135–140.
[93] I. El Moctar, Q. Ni, Y. Bai, F. Wu, C. Wu, *Funct. Mater. Lett.* **2018**, *11*, 1830003.
[94] W. Deng, Y. Cao, G. Yuan, G. Liu, X. Zhang, Y. Xia, *ACS Appl. Mater. Interfaces* **2021**, *13*, 47728–47739.
[95] G. Zhang, L. Zhang, Q. Ren, L. Yan, F. Zhang, W. Lv, Z. Shi, *ACS Appl. Mater. Interfaces* **2021**, *13*, 31650–31659.
[96] W. Shao, Q. Cao, S. Liu, T. Zhang, Z. Song, C. Song, Z. Weng, X. Jian, F. Hu, *SusMat* **2022**, *2*, 319–334.
[97] B. Zhang, C. M. Ghimbeu, C. Laberty, C. Vix-Guterl, J.-M. Tarascon, *Adv. Energy Mater.* **2016**, *6*, 1501588.
[98] A. Gomez-Martin, J. Martinez-Fernandez, M. Ruttert, M. Winter, T. Placke, J. Ramirez-Rico, *Chem. Mater.* **2019**, *31*, 7288–7299.
[99] R. Li, J. Huang, W. Li, J. Li, L. Cao, Z. Xu, Y. He, A. Yu, G. Lu, *Electrochim. Acta* **2019**, *313*, 109–115.
[100] C. Chen, Y. Huang, Y. Zhu, Z. Zhang, Z. Guang, Z. Meng, P. Liu, *ACS Sustainable Chem. Eng.* **2020**, *8*, 1497–1506.
[101] S. Alvin, C. Chandra, J. Kim, *Chem. Eng. J.* **2020**, *391*, 123576.
[102] Z. Hong, Y. Zhen, Y. Ruan, M. Kang, K. Zhou, J.-M. Zhang, Z. Huang, M. Wei, *Adv. Mater.* **2018**, *30*, e1802035.
[103] Z. Li, et al., *Adv. Energy Mater.* **2017**, *7*, 1602894.
[104] D. Wu, F. Sun, Z. Qu, H. Wang, Z. Lou, B. Wu, G. Zhao, *J. Mater. Chem. A* **2022**, *10*, 17225–17236.
[105] Y. Wang, Y. Li, S. S. Mao, D. Ye, W. Liu, R. Guo, Z. Feng, J. Kong, J. Xie, *Sustain. Energy Fuels* **2019**, *3*, 717–722.
[106] J. Figueiredo, M. Pereira, M. Freitas, J. Órfão, *Carbon* **1999**, *37*, 1379–1389.
[107] C. Matei Ghimbeu, J. Górka, V. Simone, L. Simonin, S. Martinet, C. Vix-Guterl, *Nano Energy* **2018**, *44*, 327–335.
[108] E. Olsson, J. Cottom, H. Alptekin, H. Au, M. Crespo-Ribadeneyra, M.-M. Titirici, Q. Cai, *Small* **2022**, *18*, e2200177.
[109] E. Olsson, J. Cottom, H. Au, M.-M. Titirici, Q. Cai, *Carbon* **2021**, *177*, 226–243.
[110] C. Shen, C. Wang, T. Jin, X. Zhang, L. Jiao, K. Xie, *Nanoscale* **2022**, *14*, 8959–8966.
[111] Y. Shao, et al., *Nano Lett.* **2013**, *13*, 3909–3914.
[112] D. Sun, B. Luo, H. Wang, Y. Tang, X. Ji, L. Wang, *Nano Energy* **2019**, *64*, 103937.
[113] Y. Zhao, J. Ye, P. Zhang, Z. Li, H. Zhao, *Appl. Surf. Sci.* **2022**, *602*, 154336.
[114] W. Chen, C. Chen, X. Xiong, P. Hu, Z. Hao, Y. Huang, *Adv. Sci.* **2017**, *4*, 1600500.
[115] F. Sun, H. Wang, Z. Qu, K. Wang, L. Wang, J. Gao, J. Gao, S. Liu, Y. Lu, *Adv. Energy Mater.* **2021**, *11*, 2002981.
[116] C.-X. Yu, Y. Li, Z.-H. Wang, X.-R. Wang, Y. Bai, C. Wu, *Rare Met.* **2022**, *41*, 1616–1625.
[117] M. Liu, F. Wu, Y. Gong, Y. Li, Y. Li, X. Feng, Q. Li, C. Wu, Y. Bai, *Adv. Mater.* **2023**, *35*, e2300002.
[118] L. A. Romero-Cano, H. García-Rosero, F. Carrasco-Marín, A. F. Pérez-Cadenas, L. V. González-Gutiérrez, A. I. Zárate-Guzmán, G. Ramos-Sánchez, *Electrochim. Acta* **2019**, *326*, 134973.
[119] H. Wang, F. Sun, Z. Qu, K. Wang, L. Wang, X. Pi, J. Gao, G. Zhao, *ACS Sustainable Chem. Eng.* **2019**, *7*, 18554–18565.
[120] Y. Zhang, N. Zhang, W. Chen, Z. Rao, J. Wu, L. Xue, W. Zhang, *Energy Technol.* **2019**, *7*, 1900779.
[121] H. Xie, Z. Wu, Z. Wang, N. Qin, Y. Li, Y. Cao, Z. Lu, *J. Mater. Chem. A* **2020**, *8*, 3606–3612.
[122] Y. Zhao, J. Ye, P. Zhang, Z. Li, H. Zhao, *Appl. Surf. Sci.* **2022**, *602*, 154336.
[123] N. A. Gvozdik, K. J. Stevenson, *Electrochim. Acta* **2021**, *383*, 138300.
[124] H. Radinger, F. Bauer, F. Scheiba, *Batteries & Supercaps* **2023**, *6*.
[125] a) B. M. Weckhuysen, *Chem. Commun.* **2002**, *2*, 97–110; b) M. A. Bañares, *Catal. Today* **2005**, *100*, 71–77; c) U. Caudillo-Flores, M. J. Muñoz-Batista, A. Kubacka, M. Fernández-García, *ChemPhotoChem* **2018**, *2*, 777–785; d) A. Chakrabarti, et al., *Catal. Today* **2017**, *283*, 27–53; e) B. M. Weckhuysen, *Phys. Chem. Chem. Phys.* **2003**, *5*, 4351.
[126] N. Sun, J. Qiu, B. Xu, *Adv. Energy Mater.* **2022**, *12*, 2200715.
[127] S. Alvin, H. S. Cahyadi, J. Hwang, W. Chang, S. K. Kwak, J. Kim, *Adv. Energy Mater.* **2020**, *10*, 2000283.
[128] J. R. Rodriguez, S. B. Aguirre, V. G. Pol, *Electrochim. Acta* **2019**, *319*, 791–800.
[129] a) C. Pasquini, L. D'Amario, I. Zaharieva, H. Dau, *J. Chem. Phys.* **2020**, *152*; b) H. Radinger, P. Connor, R. Stark, W. Jaegermann, B. Kaiser, *ChemCatChem* **2021**, *13*, 1175–1185; c) L. Bai, S. Lee, X. Hu, *Angew. Chem. Int. Ed.* **2021**, *60*, 3095–3103.
[130] M. Inaba, H. Yoshida, Z. Ogumi, *J. Electrochem. Soc.* **1996**, *143*, 2572–2578.
[131] M. Anji Reddy, M. Helen, A. Groß, M. Fichtner, H. Euchner, *ACS Energy Lett.* **2018**, *3*, 2851–2857.
[132] a) I. Oda, H. Ogasawara, M. Ito, *Langmuir* **1996**, *12*, 1094–1097; b) B. D. Smith, D. E. Irish, P. Kedzierzawski, J. Augustynski, *J. Electrochem. Soc.* **1997**, *144*, 4288–4296.
[133] H. Euchner, B. P. Vinayan, M. A. Reddy, M. Fichtner, A. Groß, *J. Mater. Chem. A* **2020**, *8*, 14205–14213.
[134] a) F. Tuinstra, J. L. Koenig, *J. Chem. Phys.* **1970**, *53*, 1126–1130; b) R. P. Vidano, D. B. Fischbach, L. J. Willis, T. M. Loehr, *Solid State Commun.* **1981**, *39*, 341–344.
[135] J. S. Weaving, A. Lim, J. Millichamp, T. P. Neville, D. Ledwoch, E. Kendrick, P. F. McMillan, P. R. Shearing, C. A. Howard, D. J. L. Brett, *ACS Appl. Energ. Mater.* **2020**, *3*, 7474–7484.
[136] S. Huang, Z. Li, B. Wang, J. Zhang, Z. Peng, R. Qi, J. Wang, Y. Zhao, *Adv. Funct. Mater.* **2018**, *28*, 1706294.
[137] X. Cheng, H. Li, Z. Zhao, Y. Wang, X. Wang, *New. Carbon. Mater.* **2021**, *36*, 93–105.
[138] J. M. Bray, et al., *Nat. Commun.* **2020**, *11*, 2083.
[139] K. Gotoh, T. Yamakami, I. Nishimura, H. Kometani, H. Ando, K. Hashi, T. Shimizu, H. Ishida, *J. Mater. Chem. A* **2020**, *8*, 14472–14481.
[140] a) A. Z. Weber, M. M. Mench, J. P. Meyers, P. N. Ross, J. T. Gostick, Q. Liu, *J. Appl. Electrochem.* **2011**, *41*, 1137–1164; b) K. Lourenssen, J. Williams, F. Ahmadpour, R. Clemmer, S. Tasnim, *J. Energy Storage* **2019**, *25*, 100844.
[141] a) L. Gubler, *Curr. Opin. Electrochem.* **2019**, *18*, 31–36; b) R. D. Pichugov, D. V. Konev, M. M. Petrov, A. E. Antipov, P. A. Loktionov, L. Z. Abunaeva, A. A. Usenko, M. A. Vorotyntsev, *ChemPlusChem* **2020**, *85*, 1919–1927.
[142] Z. He, Y. Lv, T. Zhang, Y. Zhu, L. Dai, S. Yao, W. Zhu, L. Wang, *Chem. Eng. J.* **2022**, *427*, 131680.
[143] K. J. Kim, M.-S. Park, Y.-J. Kim, J. H. Kim, S. X. Dou, M. Skyllas-Kazacos, *J. Mater. Chem. A* **2015**, *3*, 16913–16933.
[144] T. X. Huong Le, M. Bechelany, M. Cretin, *Carbon* **2017**, *122*, 564–591.
[145] a) A. Lindner, H. Radinger, F. Scheiba, H. Ehrenberg, *RSC Adv.* **2022**, *12*, 14119–14126; b) K. Köble, M. Jaugstetter, M. Schilling, M. Braig, T. Diemant, K. Tschulik, R. Zeis, *J. Power Sources* **2023**, *569*, 233010; c) A. M. Pezeshki, J. T. Clement, G. M. Veith, T. A. Zawodzinski, M. M. Mench, *J. Power Sources* **2015**, *294*, 333–338; d) K. V. Greco, A. Forner-Cuenca, A. Mularczyk, J. Eller, F. R. Brushett, *ACS Appl. Mater. Interfaces* **2018**, *10*, 44430–44442; e) P. C. Ghimire, R. Schweiss, G. G. Scherer, T. M. Lim, N. Wai, A. Bhattarai, Q. Yan, *Carbon* **2019**, *155*, 176–185; f) K. J. Kim, S.-W. Lee, T. Yim, J.-G. Kim, J. W. Choi, J. H. Kim, M.-S. Park, Y.-J. Kim, *Sci. Rep.* **2014**, *4*, 6906.

[146] P. Mazúr, J. Mrlík, J. Beneš, J. Pocedič, J. Vrána, J. Dundálek, J. Kosek, *J. Power Sources* **2018**, *380*, 105–114.
[147] B. Sun, M. Skyllas-Kazacos, *Electrochim. Acta* **1992**, *37*, 1253–1260.
[148] B. Sun, M. Skyllas-Kazakos, *Electrochim. Acta* **1991**, *36*, 513–517.
[149] a) B. Shanahan, K. Seteiz, P. A. Heizmann, S. Koch, J. Büttner, S. Ouardi, S. Vierrath, A. Fischer, M. Breitwieser, *RSC Adv.* **2021**, *11*, 32095–32105; b) A. Hassan, T. Tzedakis, *J. Energy Storage* **2019**, *26*, 100967.
[150] B. Sun, M. Skyllas-Kazacos, *Electrochim. Acta* **1992**, *37*, 2459–2465.
[151] Z. He, Y. Jiang, W. Meng, F. Jiang, H. Zhou, Y. Li, J. Zhu, L. Wang, L. Dai, *Appl. Surf. Sci.* **2017**, *423*, 111–118.
[152] a) W. Wang, Z. Wei, W. Su, X. Fan, J. Liu, C. Yan, C. Zeng, *Electrochim. Acta* **2016**, *205*, 102–112; b) J. Noack, N. Roznyatovskaya, J. Kunzendorf, M. Skyllas-Kazacos, C. Menictas, J. Tübke, *J. Energy Chem.* **2018**, *27*, 1341–1352.
[153] a) Z. Zhang, J. Xi, H. Zhou, X. Qiu, *Electrochim. Acta* **2016**, *218*, 15–23; b) S. Oh, C. Noh, M. Shin, Y. Kwon, *Int. J. Energy Res.* **2022**, *46*, 8803–8816.
[154] a) R.-H. Huang, C.-H. Sun, T. Tseng, W. Chao, K.-L. Hsueh, F.-S. Shieu, *J. Electrochem. Soc.* **2012**, *159*, A1579–A1586; b) L. Wei, T. S. Zhao, L. Zeng, X. L. Zhou, Y. K. Zeng, *Appl. Energy* **2016**, *180*, 386–391; c) W. H. Wang, X. D. Wang, *Electrochim. Acta* **2007**, *52*, 6755–6762; d) Y. Xiang, W. A. Daoud, *Electrochim. Acta* **2018**, *290*, 176–184; e) D. J. Suárez, Z. González, C. Blanco, M. Granda, R. Menéndez, R. Santamaría, *ChemSusChem* **2014**, *7*, 914–918.
[155] a) D. M. Kabtamu, Y.-C. Chang, G.-Y. Lin, A. W. Bayeh, J.-Y. Chen, T. H. Wondimu, C.-H. Wang, *Sustain. Energy Fuels* **2017**, *1*, 2091–2100; b) A. W. Bayeh, D. M. Kabtamu, Y.-C. Chang, G.-C. Chen, H.-Y. Chen, G.-Y. Lin, T.-R. Liu, T. H. Wondimu, K.-C. Wang, C.-H. Wang, *ACS Sustainable Chem. Eng.* **2018**, *6*, 3019–3028; c) Y. Xiang, W. A. Daoud, *J. Electrochem. Soc.* **2017**, *164*, A2256–A2261; d) X. Wu, H. Xu, L. Lu, H. Zhao, J. Fu, Y. Shen, P. Xu, Y. Dong, *J. Power Sources* **2014**, *250*, 274–278.
[156] a) Y. Lv, Y. Yang, J. Gao, J. Li, W. Zhu, L. Dai, Y. Liu, L. Wang, Z. He, *Electrochim. Acta* **2022**, *431*, 141135; b) Z. González, C. Flox, C. Blanco, M. Granda, J. R. Morante, R. Menéndez, R. Santamaría, *J. Power Sources* **2017**, *338*, 155–162; c) M. Kim, J. Park, G. Yeo, M. Ko, H. Jang, *Carbon* **2023**, *206*, 1–6.
[157] J. Maruyama, S. Maruyama, T. Fukuhara, K. Hanafusa, *J. Phys. Chem. C* **2017**, *121*, 24425–24433.
[158] J. Langner, M. Bruns, D. Dixon, A. Nefedov, C. Wöll, F. Scheiba, H. Ehrenberg, C. Roth, J. Melke, *J. Power Sources* **2016**, *321*, 210–218.
[159] H. Fink, J. Friedl, U. Stimming, *J. Phys. Chem. C* **2016**, *120*, 15893–15901.
[160] Y. Long, M. Ding, C. Jia, *ChemNanoMat* **2021**, *7*, 699–712.
[161] a) R. M. Bachman, D. M. Hall, L. R. Radovic, *Carbon* **2023**, *201*, 891–899; b) Y. Li, J. Parrondo, S. Sankarasubramanian, V. Ramani, *J. Phys. Chem. C* **2019**, *123*, 6370–6378; c) P. Leuaa, D. Priyadarshani, A. K. Tripathi, M. Neergat, *J. Electroanal. Chem.* **2020**, *878*, 114590; d) H. Radinger, J. Pfisterer, F. Scheiba, H. Ehrenberg, *ChemElectroChem* **2020**, *7*, 4745–4754; e) J. Friedl, C. M. Bauer, A. Rinaldi, U. Stimming, *Carbon* **2013**, *63*, 228–239.
[162] A. K. Singh, N. Yasri, K. Karan, E. P. L. Roberts, *ACS Appl. Energ. Mater.* **2019**, *2*, 2324–2336.
[163] H. Kim, J. S. Yi, D. Lee, *ACS Appl. Energ. Mater.* **2021**, *4*, 425–433.
[164] a) M. Park, I.-Y. Jeon, J. Ryu, J.-B. Baek, J. Cho, *Adv. Energy Mater.* **2015**, *5*, 1401550; b) Y. Jiang, G. Cheng, Y. Li, Z. He, J. Zhu, W. Meng, H. Zhou, L. Dai, L. Wang, *Appl. Surf. Sci.* **2020**, *525*, 146453; c) M. Jing, Y. Yang, Z. Liu, X. Ma, D. Fang, X. Fan, J. Liu, C. Yan, *J. Electrochem. Soc.* **2021**, *168*, 60533.
[165] S.-C. Kim, H. Lim, H. Kim, J. S. Yi, D. Lee, *Electrochim. Acta* **2020**, *348*, 136286.
[166] J. Kim, H. Lim, J.-Y. Jyoung, E.-S. Lee, J. S. Yi, D. Lee, *Electrochim. Acta* **2017**, *245*, 724–733.
[167] S. Bellani, et al., *Chem. Mater.* **2021**, *33*, 4106–4121.
[168] A. Xu, L. Shi, L. Zeng, T. S. Zhao, *Electrochim. Acta* **2019**, *300*, 389–395.
[169] Y. Shao, X. Wang, M. Engelhard, C. Wang, S. Dai, J. Liu, Z. Yang, Y. Lin, *J. Power Sources* **2010**, *195*, 4375–4379.
[170] a) L. Yu, F. Lin, L. Xu, J. Xi, *J. Energy Chem.* **2019**, *35*, 55–59; b) Z. Jialin, L. Yiyang, L. Shanfu, X. Yan, *Batteries* **2023**, *9*, 40; c) H. Radinger, M. Hartmann, M. Ast, J. Pfisterer, M. Bron, H. Ehrenberg, F. Scheiba, *Electrochim. Acta* **2022**, *409*, 139971.
[171] H. Gursu, M. Gencten, Y. Sahin, *J. Electrochem. Soc.* **2021**, *168*, 60504.
[172] a) C. Li, B. Xie, J. Chen, J. He, Z. He, *RSC Adv.* **2017**, *7*, 13184–13190; b) M. G. Ersozoglu, H. Gursu, M. Gencten, A. S. Sarac, Y. Sahin, *Int. J. Energy Res.* **2021**, *45*, 2126–2137; c) M. G. Ersozoglu, H. Gursu, M. Gencten, A. S. Sarac, Y. Sahin, *Int. J. Energy Res.* **2022**, *46*, 19992–20003.
[173] a) Y. Huang, Q. Deng, X. Wu, S. Wang, *Int. J. Hydrogen Energy* **2017**, *42*, 7177–7185; b) O. Di Blasi, N. Briguglio, C. Busacca, M. Ferraro, V. Antonucci, A. Di Blasi, *Appl. Energy* **2015**, *147*, 74–81; c) W. Zhang, J. Xi, Z. Li, H. Zhou, Le Liu, Z. Wu, X. Qiu, *Electrochim. Acta* **2013**, *89*, 429–435; d) L. Yue, W. Li, F. Sun, L. Zhao, L. Xing, *Carbon* **2010**, *48*, 3079–3090.

Manuscript received: September 29, 2023
Revised manuscript received: November 14, 2023
Version of record online: ■■, ■■

REVIEW

Sodium-ion and vanadium flow batteries: Understanding the impact of defects in carbon-based materials is a critical step for the widespread application of sodium-ion and vanadium flow batteries as high-performance and cost-effective energy storage systems. In this review, various techniques for achieving such defect structural properties are presented, followed by an outline of their impact on the respective storage system.

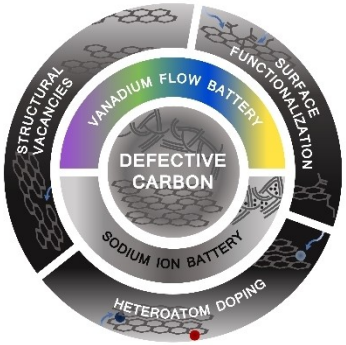

S. McArdle, F. Bauer, S. F. Granieri, M. Ast, Dr. F. Di Fonzo, Prof. Dr. A. T. Marshall, Dr. H. Radinger**

1 – 26

Defective Carbon for Next-Generation Stationary Energy Storage Systems: Sodium-Ion and Vanadium Flow Batteries